

## Leveraging motional-mode balancing and simply parametrized waveforms to perform frequency-robust entangling gates

Brandon P. Ruzic<sup>1,\*</sup>, Matthew N.H. Chow<sup>1,2,3,†</sup>, Ashlyn D. Burch<sup>1</sup>, Daniel S. Lobser<sup>1</sup>,  
Melissa C. Revelle<sup>1</sup>, Joshua M. Wilson<sup>1</sup>, Christopher G. Yale<sup>1</sup> and Susan M. Clark<sup>1</sup>

<sup>1</sup>*Sandia National Laboratories, Albuquerque, New Mexico 87185, USA*

<sup>2</sup>*Department of Physics and Astronomy, University of New Mexico, Albuquerque, New Mexico 87106, USA*

<sup>3</sup>*Center for Quantum Information and Control, University of New Mexico, Albuquerque, New Mexico 87131, USA*

 (Received 29 November 2022; revised 10 May 2024; accepted 21 May 2024; published 2 July 2024)

Near-term quantum algorithms require high-performance entangling gates in a scalable quantum processor, and Mølmer-Sørensen (MS) gates on trapped ions have achieved some of the highest entanglement fidelities to date. However, technical noise that induces small changes in the motional frequencies of the ion chain is a dominant error source in these gates that limits scalability. Here, we report an improved MS-gate design that mitigates the impact of motional-frequency changes by using a class of laser waveforms with three salient features: a spectrally compact Fourier transform, a constant frequency that balances contributions to the MS-gate rotation angle from all motional modes, and a simple parameterization. Together, these features suppress residual coherent displacement of the motional modes, generate robustness to rotation-angle error, and provide low technical complexity and computational overhead. As a proof of concept, we implement this gate design on a four-ion chain, achieving a <1% fidelity reduction over a  $\pm 10$  kHz range of frequency offset from the calibrated detuning. We also analyze the applicability of our gate design to longer ion chains through numerical simulations of our gate design on chains of up to 33 ions. This robustness to motional-frequency changes represents an order-of-magnitude improvement over the more complicated waveform-shaping techniques that currently dominate the robust-gate literature, and our simulations predict that a high level of robustness can be maintained in these systems for longer ion chains. In addition, the robustness and simplicity of our approach promises to accelerate the development of quantum architectures that invoke long algorithmic runtimes and frequent calibration.

DOI: [10.1103/PhysRevApplied.22.014007](https://doi.org/10.1103/PhysRevApplied.22.014007)

### I. INTRODUCTION

Quantum computers have the potential to perform powerful algorithms, like digital quantum simulation [1] and quantum error correction [2–4], and linear chains of trapped ions provide one of the most promising platforms for quantum computation in the near term. The application of Mølmer-Sørensen (MS) gates [5] in these systems has produced some of the highest two-qubit entanglement fidelities to date, reaching above 99.9% with two-ion chains [6–8], and encouraging results have been obtained in larger systems. For example, a fidelity of 98.5–99.3% has been achieved on all pairs of ions in a 32-ion chain, enabling the production of an error-corrected logical qubit [9], and an average entanglement fidelity of 99.8% has been achieved across four interaction regions in the quantum

charge-coupled device (QCCD) architecture [10,11], enabling the best measurement of quantum volume to date ( $2^{19}$ ), in a system of 120 qubits [12].

However, trapped-ion processors require more qubits and even higher fidelities to perform near-term algorithms, and technical noise that alters the motional frequencies of the ions is one of the biggest barriers preventing high-fidelity MS gates at larger scales. For short chains in the QCCD architecture, high-fidelity MS gates require calibration to the precise values of the motional frequencies in the interaction regions, and these frequencies must be stabilized over the course of an algorithm. For longer-chain architectures, high-fidelity operations require this type of calibration and stabilization for an increasing number of motional modes and for each pair of ions. Moreover, the increasing spectral density of motional modes in longer chains increases the sensitivity to changes in the motional frequencies.

Two different types of MS-gate error can emerge from motional-frequency changes. The first type of gate error

\*Contact author: [bruzic@sandia.gov](mailto:bruzic@sandia.gov)

†Contact author: [mnchow@sandia.gov](mailto:mnchow@sandia.gov)

comes from residual motional displacement after the gate (i.e., displacement error). This displacement causes the motion of the ions to be entangled with their spin after the gate, leading to a (mostly) incoherent gate error after tracing out the motional degrees of freedom [13]. The second type of gate error comes from obtaining the incorrect value of gate rotation angle (i.e., rotation-angle error). This error is a purely coherent gate error, which is especially damaging to the performance of quantum algorithms that involve many gates [14]. For example, the circuit sensitivity to rotation error has been demonstrated through the repeated application of MS gates on two-ion and four-ion chains [15].

Consequently, researchers have attempted a range of techniques to mitigate the effects of motional-frequency changes. Most techniques involve modulating the laser beams that drive the MS gate, including amplitude modulation [16–23], frequency modulation [15,24], simultaneous amplitude and frequency modulation [25–29], and phase modulation [30–32]. Alternative techniques involve the application of additional laser tones [33,34]. These techniques eliminate all gate error in ideal experimental conditions and add various degrees of robustness against gate errors upon motional-frequency changes.

Nevertheless, motional-frequency changes continue to be a dominant source of error in high-fidelity gates [15]. This error source persists, in part, because most approaches mitigate the effects of motional-frequency changes by providing robustness to displacement error [24,26,28], without explicitly providing robustness to rotation-angle error. More recent attempts to simultaneously reduce both displacement error and rotation-angle error have achieved some gains [29,35,36], but rotation-angle error still tends to dominate over displacement error in these approaches, leading to significant coherent gate error.

Critically, as system sizes increase, technical complications further limit the ability to mitigate motional-frequency changes and perform high-fidelity gates. For short chains in the QCCD architecture, larger systems require a greater amount of ion shuttling and recoiling that increases the total runtime of quantum algorithms, making these systems more susceptible to motional-frequency drift. In addition, any residual motional excitation increases the sensitivity to motional-frequency changes [13]. In longer-chain architectures, the majority of frequency-robust gate designs require a number of optimized waveform parameters that increases linearly with the number of ions, making these techniques more difficult to implement as the length of the chain increases [24]. Some approaches limit the number of waveform parameters by only targeting closely spaced ions or by using spectrally compact waveforms [22,25–27], but these techniques still have strict experimental requirements that grow

with the number of ions. For example, modulated gates on longer ion chains require larger laser powers [15,26] and generally have a higher sensitivity to changes in the calibrated model parameters (e.g., motional frequencies, ion separation, laser power, and gate duration) [35]. As a result, in both QCCD and longer-chain architectures, larger systems are more susceptible to motional-frequency changes, require more frequent calibration, and would benefit from strongly robust gates that are easy and efficient to implement.

Therefore, we propose an alternative MS-gate design that mitigates the impact of motional-frequency changes by using a class of waveforms with three salient features. The first feature is a spectrally compact Fourier transform that strongly suppresses displacement error in all motional modes, as long as the detuning from each mode remains sufficiently large. The second feature is a specific, constant laser detuning that balances the contribution to the rotation angle from all modes, providing strong robustness to rotation-angle error. We choose this detuning such that the first derivative of the gate rotation angle with respect to detuning goes to zero, and we are free to adjust (or calibrate) this detuning without adding significant displacement error. This method of mode balancing produces a gate that is not only first-order insensitive to detuning but also has a significantly reduced second-order derivative with respect to detuning, as compared to many other gate designs, resulting in broad regions of robustness to motional-frequency changes, even for longer ion chains. The third feature of this class of waveforms is a simple parameterization that removes the need to optimize a large set of waveform parameters but yet still provides broad robustness to motional-frequency changes. With a simply parameterized waveform, our gate design is exceedingly simple to realize experimentally; we can optimize performance by calibrating only two waveform parameters: the constant detuning and the peak Rabi rate. As a result, our MS gate design is quick to calibrate and has a low classical computational overhead, facilitating its adoption on trapped-ion quantum processors throughout the scientific community and making our gate design suitable for systems suffering from even substantial amounts of drift.

As a proof of concept, we demonstrate the motional-frequency robustness of our gate design on a four-ion chain on the Quantum Scientific Computing Open User Testbed, QSCOUT. We use qubits encoded in the hyperfine clock states of  $^{171}\text{Yb}^+$  ions trapped in a linear chain above a surface-electrode trap. Gates are site selectively driven with an optical Raman transition. Details of the apparatus are described in this previous work [37]. In addition, we analyze the robustness of our gate design to motional-frequency changes through numerical simulations of our gate design on chains of up to 33 ions and for various ion separations.

## II. GATE DESIGN

### A. MS gate model

We model the application of an MS gate on two ions that are part of a linear chain of trapped ions using the Hamiltonian,

$$H(t) = -\Omega(t) \sum_k S_{y,k} a_k e^{i\delta_k t} + \text{h.c.}, \quad (1)$$

which is in a rotating frame with respect to the internal and motional degrees of freedom. This Hamiltonian arises from using a system of counterpropagating laser beams to generate two Raman tones on each target ion. For a chain  $N$  ions, the sum over  $k$  includes  $2N$  radial motional modes, for  $\{k : 0 \dots 2N - 1\}$  in order of increasing energy. The operator  $a_k^\dagger$  ( $a_k$ ) is the raising (lowering) operator of a harmonic oscillator that represents the  $k$ th motional mode of the chain with angular frequency  $\nu_k$ . As shown by the blue (red) vertical dashed line in Fig. 1, the blue-detuned (red-detuned) Raman tone has a detuning of  $\delta_c$  ( $-\delta_c$ ) from the carrier transition between the ground and excited spin states,  $|0\rangle$  and  $|1\rangle$ , respectively, where  $\delta_c > 0$ . As a result, the blue-detuned (red-detuned) tone is detuned by  $\delta_k$  ( $-\delta_k$ ) from the blue (red) motional sideband transition of mode  $k$ , where  $\delta_k = \delta_c - \nu_k$ . The blue (red) sideband transition corresponds to causing a spin flip from  $|0\rangle$  to  $|1\rangle$  and increasing (decreasing) the motion in mode  $k$  by one phonon. For a gate targeting ions  $j_1$  and  $j_2$  in the chain, the collective spin operator  $S_{y,k}$  has the form:  $S_{y,k} = (\eta_{j_1,k} \sigma_{y,j_1} + \eta_{j_2,k} \sigma_{y,j_2})/2$ , where  $\sigma_{y,j}$  is the  $y$  Pauli spin operator for the  $j$ th ion. The Lamb-Dicke parameter  $\eta_{j,k}$  can differ for each ion and each motional mode, and the Rabi rate of the carrier transition  $\Omega(t)$  is the same for both targeted ions. In this work,  $\Omega(t)$  is a time-dependent parameter of the drive field, and  $\delta_k$  is held constant in time for each mode. For simplicity, we have made the Lamb-Dicke approximation:  $e^{i\eta_{j,k}(a_k + a_k^\dagger)} \approx 1 + i\eta_{j,k}(a_k + a_k^\dagger)$ . We have also neglected the carrier transition and far-off-resonant sideband transitions, including those from axial motion.

Since the Hamiltonian  $H(t)$  acts on each motional mode independently, we can write the propagator  $U(t)$  as a product over motional modes:

$$U(t) = \prod_k U_k(t), \quad (2)$$

and the exact analytic solution for  $U_k(t)$  is [5,13],

$$U_k(t) = e^{-i\mathcal{B}_k(t)S_{y,k}^2} D(S_{y,k}\alpha_k(t)),$$

$$\mathcal{B}_k(t) = \frac{i}{2} \int_0^t \left( \frac{d\alpha_k(t')}{dt'} \alpha_k^*(t') - \alpha_k(t') \frac{d\alpha_k^*(t')}{dt'} \right) dt'. \quad (3)$$

The displacement operator  $D(S_{y,k}\alpha_k(t)) = \exp[S_{y,k}(\alpha_k(t)a_k^\dagger - \alpha_k^*(t)a_k)]$  is conditioned on the spin

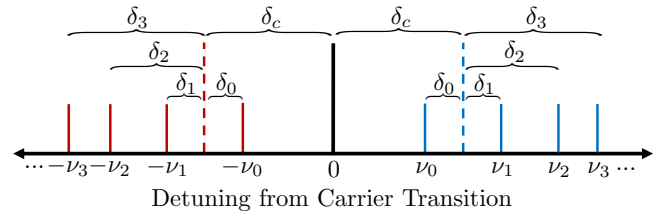


FIG. 1. Spectral diagram of Raman detunings (not to scale) for an MS gate with the contributions to its rotation angle balanced between all motional modes, while primarily targeting the two lowest-energy modes. A chain of  $N$  ions has  $2N$  radial modes, indexed here by  $k$  for  $\{k : 0 \dots 2N - 1\}$  in order of increasing energy, but only four modes are shown for clarity. Mode  $k$  has frequency  $\nu_k/2\pi$ . The black vertical line represents the carrier transition between the ground and excited spin states,  $|0\rangle$  and  $|1\rangle$ , respectively. The blue (red) vertical solid line at  $\nu_k$  ( $-\nu_k$ ) represents the blue (red) motional sideband transition of mode  $k$ , which corresponds to causing a spin flip from  $|0\rangle$  to  $|1\rangle$  and increasing (decreasing) the motion in mode  $k$  by one phonon. The blue (red) vertical dashed line represents the detuning  $\delta_c$  ( $-\delta_c$ ) of the blue-detuned (red-detuned) Raman tone from the carrier transition, where  $\delta_c > 0$ . As a result, the blue-detuned (red-detuned) Raman tone is detuned by  $\delta_k$  ( $-\delta_k$ ) from the blue (red) motional sideband transition of mode  $k$ , where  $\delta_k = \delta_c - \nu_k$ .

state of the targeted ions, and  $\alpha_k(t)$  describes the phase-space trajectory of the ion chain. The phase  $\eta_{j_1,k}\eta_{j_2,k}\mathcal{B}_k(t)$ , which governs the amount of spin entanglement accrued during the gate, is real and positive (negative) for clockwise (counterclockwise) trajectories.

To gain an intuitive picture of the gate dynamics, we express the phase-space trajectory of each motional mode in terms of the parameters of  $H(t)$ ,

$$\alpha_k(t) = i \int_0^t \Omega(t') e^{-i\delta_k t'} dt', \quad (4)$$

where  $t = \tau$  corresponds to the end of the gate. From this equation, we see that  $\alpha_k(\tau)$  is proportional to the Fourier transform of  $\Omega(t)$  evaluated at  $\delta_k$ , assuming that  $\Omega(t)$  is zero before ( $t < 0$ ) and after ( $t > \tau$ ) the gate [23]. This is a key insight that will aid our choice of waveform for frequency-robust gates, as discussed in Sec. II C.

In this study, we focus on the robustness of MS-gate performance to a frequency offset  $\delta\omega/2\pi$  that is applied to both laser tones and moves them symmetrically with respect to the carrier transition, resulting in shifted carrier detunings:  $\pm\delta'_c = \pm(\delta_c + \delta\omega)$  and sideband detunings:  $\pm\delta'_k = \pm(\delta_k + \delta\omega)$ . We consider values of  $|\delta\omega|$  that can significantly alter the sideband detunings but have a negligible effect on the Lamb-Dicke parameters. For this reason, we keep the Lamb-Dicke parameters fixed in our model but allow the sideband detunings to change with  $\delta\omega$ . This causes  $\delta\omega/2\pi$  to be equivalent to a common change in the motional frequency of each mode:  $\nu'_k = \nu_k - \delta\omega$ , allowing us to use  $\delta\omega$  as a proxy for motional frequency changes in

this study. Although other error sources can affect gate performance, such as laser power fluctuations and anomalous heating [38,39], we choose to focus on motional frequency changes due to the high sensitivity of gate performance to this effect [13], especially in the context of longer ion chains with many closely spaced motional modes.

## B. Performance metrics

We use the state fidelity  $\mathcal{F}$  as the figure of merit for gate performance, which can be computed by wave-function overlap:

$$\mathcal{F} = |\langle \Phi | \Psi(\tau) \rangle|^2, \quad (5)$$

where  $|\Psi(\tau)\rangle$  is the wave function of the ion chain at the end of the gate and  $|\Phi\rangle$  is the target state. We assume that we perfectly initialize the ions in the spin state  $|00\rangle$  and laser cool them to reach the motional ground state  $|0\rangle$ . The state of the ion chain after the gate is then  $|\Psi(\tau)\rangle = \prod_k e^{iB_k(\tau)S_{y,k}^2} D(S_{y,k}\alpha_k(\tau)) |00, 0\rangle$ , and we choose to target the state  $|\phi\rangle = 1/\sqrt{2}(|00\rangle + i|11\rangle) |0\rangle$ , a maximally entangled spin state and the motional ground state. Although we will focus on the state fidelity for the initial spin state  $|00\rangle$  and report experimental measurements of this state fidelity in Sec. III C, we note that in our simulations this metric is representative of the entanglement fidelity, which is a measure of the average fidelity for all initial spin states [40]. Hence, the state fidelity acts as a sufficient metric to quantify gate performance in this paper.

For ideal gate performance ( $\mathcal{F} = 1$ ), we require the propagator at the end of the gate ( $t = \tau$ ) to take the following form:  $U(\tau) = e^{-i\sigma_y j_1 \sigma_y j_2 \theta/2}$ , where  $\theta$  is the rotation angle of the gate. For our choice of initial and final states, the ideal gate is accomplished for,

$$\alpha_k(\tau) = 0 \quad \text{for each } k, \quad (6a)$$

$$\theta = \sum_k \eta_{j_1,k} \eta_{j_2,k} \mathcal{B}_k(\tau) = \pi/2. \quad (6b)$$

Although  $\mathcal{F}$  is a sufficient metric for gate performance, we find it illustrative for this work to decompose the state fidelity into two contributing terms: displacement error  $\epsilon_d$  and rotation-angle error  $\epsilon_r$ , which arise from inequalities in Eqs. (6a) and (6b), respectively. In the next two sections, we derive the contribution to the state infidelity  $1 - \mathcal{F}$  from each error separately, where the sum of these errors,

$$\epsilon_s = \epsilon_d + \epsilon_r, \quad (7)$$

is approximately equal to the state infidelity:  $\epsilon_s \approx 1 - \mathcal{F}$ , for small errors ( $\epsilon_d \ll 1$  and  $\epsilon_r \ll 1$ ).

## 1. Displacement error

Displacement error occurs when the coherent displacement at the end of the gate is nonzero,  $\alpha_k(\tau) \neq \alpha(0) = 0$ , and leads to residual spin-motion entanglement. In the phase-space trajectory picture, a gate with no displacement error for a particular mode will produce a closed curve, and any residual displacement (or open curve) contributes to the gate error. We call this contribution the displacement error  $\epsilon_{d,k}$  for mode  $k$ . As accomplished in several previous works, including Refs. [21–24,32,35], we design gates for which  $\epsilon_{d,k}$  is robust to motional frequency changes by shaping the laser waveform.

We derive an expression for the displacement error from each mode by acting the displacement operator for the gate on the initial state and computing the wave-function overlap with the target state:  $\mathcal{O}_{d,k} = \langle \Phi | D(S_{y,k}\alpha_k(\tau)) |00, 0\rangle$ . The operator  $S_{y,k}$  has four eigenvalues:  $\lambda_{++} = (\eta_{j_1,k} + \eta_{j_2,k})/2$ ,  $\lambda_{+-} = (\eta_{j_1,k} - \eta_{j_2,k})/2$ ,  $\lambda_{-+} = (\eta_{j_2,k} - \eta_{j_1,k})/2$ , and  $\lambda_{--} = -(\eta_{j_1,k} + \eta_{j_2,k})/2$ , corresponding to the spin states  $|++\rangle$ ,  $|+-\rangle$ ,  $| -+\rangle$ , and  $|--\rangle$ , respectively, where  $\{|+\rangle = (|0\rangle + |1\rangle)/\sqrt{2}, |-\rangle = (|1\rangle - |0\rangle)/\sqrt{2}\}$ . In terms of these eigenvalues,

$$\mathcal{O}_{d,k} = \frac{1}{4} \sum_{\lambda} e^{-|\lambda\alpha_k(\tau)|^2/2}, \quad (8)$$

and the total displacement error is,

$$\epsilon_d = \sum_k \epsilon_{d,k}, \quad (9a)$$

$$\epsilon_{d,k} = 1 - \left| \frac{1}{4} \sum_{\lambda} e^{-|\lambda\alpha_k(\tau)|^2/2} \right|^2. \quad (9b)$$

For example, if the Lamb-Dicke parameters were equal for each ion and mode involved in the gate ( $\eta_{j_1,k} = \eta_{j_2,k} = \eta$ ), then the eigenvalues of  $S_{y,k}$  would be  $\lambda = \{\eta, 0, 0, -\eta\}$ , and from Eq. (9b), we would find that  $\epsilon_{d,k} \approx \eta^2 |\alpha_k(\tau)|^2/2$  for small errors. In addition, if we were to adjust the magnitude of the target rotation angle from  $|\theta| = \pi/2$  to  $|\theta| = |\theta_{\text{target}}|$  by scaling the magnitude of  $\Omega(t)$ , we would find that  $\epsilon_d \propto |\theta_{\text{target}}|$  for small errors.

## 2. Rotation-angle error

Rotation-angle error  $\epsilon_r$  is the error in the amount of entanglement accumulated at the end of the gate. In the phase-space trajectory picture, this can be visualized as the area enclosed by the curves. Most gate designs do not explicitly target solutions that are robust to rotation-angle error caused by motional frequency drift. In this work, we utilize the contributions from multiple motional modes in order to derive a gate for which  $\epsilon_r$  is independent of motional frequency changes to first order.

We derive an expression for the rotation error by acting the spin-entangling operator for the gate on the initial state and computing the wave-function overlap with the target state:  $\mathcal{O}_r = \langle \Phi | \Pi_k e^{i\mathcal{B}_k(\tau)\delta_k^2} |00, 0\rangle$ . Since the spin-entangling operator is independent of the motional state, we only require that the rotation angle of the gate  $\theta = \sum_k \eta_{j_1,k} \eta_{j_2,k} \mathcal{B}_k(\tau)$  is equal to  $\pi/2$  to achieve an MS gate, as shown in Eq. (6b). Therefore, any deviation of this angle  $\delta\theta = \theta - \pi/2$  results in the rotation  $\delta U = e^{i\delta\theta \sigma_{y,j_1} \sigma_{y,j_2}/2}$  of the target state, up to an arbitrary global phase, and the rotation error is,

$$\epsilon_r = 1 - |\langle \Phi | \delta U | \Phi \rangle|^2 \approx \frac{1}{4} |\delta\theta|^2, \quad (10)$$

for  $|\delta\theta| \ll 1$ . In addition, if we were to scale the magnitude of  $\Omega(t)$  to adjust the target rotation angle from  $|\theta| = \pi/2$  to  $|\theta_{\text{target}}|$ , we would find that  $\epsilon_r \propto |\theta_{\text{target}}|^2$  for small errors.

### C. Amplitude modulation

The robustness of our gate design to motional frequency changes relies on a spectrally compact laser waveform. To this end, we implement spectrally compact amplitude modulation during the gate, which we describe by a time-dependent Rabi rate  $\Omega(t)$ . From Sec. II B 1, we see that the state infidelity grows linearly with the residual displacement of each mode  $|\alpha_k(\tau)|^2$ . To reduce these contributions, we note that  $\alpha_k(\tau)$  is proportional to the Fourier transform of  $\Omega(t)$  evaluated at  $\delta_k$ , as seen in Sec. II A, and we choose to perform amplitude modulation with a truncated-Gaussian shape,

$$\Omega(t) = \begin{cases} \Omega_0 e^{-(t-\tau/2)^2/2z^2}, & \text{if } 0 \leq t \leq \tau, \\ 0, & \text{otherwise,} \end{cases} \quad (11)$$

where  $\Omega_0$  is the peak Rabi rate, and  $z$  is the standard deviation (i.e., Gaussian width).

To understand the effect of the Gaussian-like amplitude modulation, we assume that  $z$  is sufficiently small ( $z^2 \ll \tau^2$ ) such that we can ignore the truncation of  $\Omega(t)$  and extend the limits of integration in Eq. (4) for  $\alpha(\tau)$  to all times,

$$\alpha_k(\tau) \approx i \int_{-\infty}^{\infty} \Omega'(t') e^{-i\delta_k t'} dt', \quad (12a)$$

$$|\alpha_k(\tau)|^2 \approx 2\pi \Omega_0^2 z^2 e^{-\delta_k^2 z^2}, \quad (12b)$$

where  $\Omega'(t) = \Omega_0 e^{-(t-\tau/2)^2/2z^2}$  for all  $t$ . Here, we see that the Gaussian-like modulation guarantees that the displacement error from each mode will exponentially decay with  $\delta_k^2$  [23]. For the appropriate choice of detuning, this can strongly suppress contributions to  $\epsilon_d$  from the modes primarily driving the gate and almost entirely eliminate

contributions to  $\epsilon_d$  from far-detuned ‘‘spectator’’ modes. Despite this strong suppression of displacement errors at the end of the gate, the maximum displacement in mode  $k$  during the gate  $\max_t(|\alpha_k(t)|)$  is only suppressed by a factor of  $1/\delta_k$  when  $|\delta_k| \gg z^{-1}$ . Likewise, the contribution from mode  $k$  to the gate rotation angle  $\theta$  scales like  $\theta_k \propto \Omega_0^2/\delta_k$  for  $|\delta_k| \gg z^{-1}$ .

### D. Mode balancing

Many MS-gate implementations, including the standard gate with a constant detuning and Rabi rate [5], suffer from the displacement error  $\epsilon_d$  caused by spectator modes, and the gate performance degrades when the detuning of the mode primarily targeted by the gate has a similar magnitude as the detuning from the other modes. However, since the Gaussian amplitude modulation strongly suppresses  $\epsilon_d$ , as discussed in Sec. II C, we have the freedom to detune close to multiple modes without suffering from large displacement errors. In this section, we take advantage of this freedom and determine a choice of detuning  $\delta_c$  that not only maintains the suppression of  $\epsilon_d$  but also reduces the rotation-angle error  $\epsilon_r$ .

While staying sufficiently far away from all modes ( $\delta_k \gg z^{-1}$ ) to suppress  $\epsilon_d$ , we aim to balance the contributions to  $\theta$  from all modes, such that motional frequency changes that increase the contribution to  $\theta$  from some modes are cancelled to first-order by the decrease in the contribution to  $\theta$  from the other modes. In general, we can determine the detunings that balance the contributions to  $\theta$  from all modes by numerically solving the following equation for  $\delta_c$ :

$$\frac{d\theta}{d\delta_c} = \sum_k \eta_{j_1,k} \eta_{j_2,k} \frac{d\mathcal{B}_k(\tau)}{d\delta_c} = 0, \quad (13)$$

which may have multiple solutions. Since this equation is a sum of one-dimensional integrals with a number of terms that grows linearly with ion number, the time to numerically solve this equation for tens of ions is only a few seconds on a typical laptop.

After solving Eq. (13) for  $\delta_c$ , we then use this value to implement an MS gate for which  $\epsilon_r$  is first-order robust to motional frequency changes. In addition, we find that this motional mode balancing can suppress the magnitude of the second-order derivative  $|d^2\theta/d\delta_c^2|$  at the balance point. As a result, this derivative can be much smaller than for numerically optimized waveforms, which typically minimize the first-order derivative at the expense of enlarging higher-order derivatives. While some numerically optimized gate designs in the literature allow one to cancel higher-order terms, these techniques add more computational overhead and often require larger laser powers. In contrast, the balanced-gate design suppresses higher-order derivatives without numerical optimization nor enhanced laser-power requirements.

To provide intuition on the solutions to Eq. (13), we note that the  $k$ th term in the sum becomes large near  $\delta_k = 0$  and tends to dominate all other terms. Also, in the region of  $\delta_c$  between two neighboring modes  $k_1$  and  $k_2$ , the quantities  $d\mathcal{B}_{k_1}/d\delta_c$  and  $d\mathcal{B}_{k_2}/d\delta_c$  have the same sign. For these reasons, a solution to Eq. (13) is likely to be found between neighboring modes when the products  $\eta_{j_1,k_1}\eta_{j_2,k_1}$  and  $\eta_{j_1,k_2}\eta_{j_2,k_2}$  have opposite signs.

Although numerically solving Eq. (13) is straightforward and efficient, it may be useful to determine values of  $\delta_c$  experimentally. In practice, one can identify regions where solutions are likely to exist and experimentally calibrate  $\delta_c$  as we describe in Sec. III C. In addition, since the solution to Eq. (13) depends on the motional frequencies, small changes in these frequencies can cause a shift in the balance point on the same scale. In this case, instead of remeasuring the motional frequencies, one can regain maximum frequency robustness by simply scanning the laser frequency and finding the value at which  $\theta$  (easily inferred from population measurements) is flat with respect to frequency. Implementing this procedure takes only a few minutes (depending on the frequency spacing between the closest two modes), and we find approximately the same balance point as solving Eq. (13) with the updated motional frequencies. Empirically determined balance points of this kind have been used to generate spin-spin Ising interactions and perform entangling gates on trapped ions [41].

Although the contribution to the rotation angle from distant modes will be suppressed by their larger detunings, we purposely include a sum over all modes in Eq. (13). Since the contribution to the rotation angle from each mode has a fairly slow decay  $\theta_k \propto 1/\delta_k$ , distant modes are likely to contribute in longer chains due to their increased spectral density. Moreover, because  $\theta_k \propto \eta_{j_1,k}\eta_{j_2,k}$ , distant modes with larger Lamb-Dicke parameters than the closest two modes make an enhanced contribution to  $\theta$  and may play a key role in the gate. By including all modes, our design applies to an arbitrary mode structure, including densely spaced and irregularly spaced spectra.

Even though Eq. (13) applies to constant frequency offsets for each mode,  $\delta'_k = \delta_c - \nu_k + \delta\omega$ , one can generalize this equation for previously known mode-dependent changes in the detunings,  $\delta_k(s) = \delta_c - \nu_k + \delta\omega_k(s)$ , by replacing  $\delta_c$  with  $s$ . We also note that while the detuning from each mode does not depend on time in this equation, one could employ the concept of motional-mode balancing to formulate a cost function for the design of frequency-modulated gates that achieve the same first-order robustness to motional frequency changes.

At least for monospecies ion chains, solutions to Eq. (13) exist for all pairs of ions and for all chain lengths. However, for chains with an odd number of ions, the center ion has a zero Lamb-Dicke parameter for many modes. In this case, the values of detuning that solve this equation can

be close to resonant with another motional mode in which the center ion does not participate but the other ion does, potentially adding an unacceptable amount of displacement error to the gate. Hence, to address the center ion with our gate design, it may be advantageous to increase the chain length by one, such that all ions have a nonzero Lamb-Dicke parameter. Alternatively, one could adjust the trapping potential to create a balance point between modes from orthogonal principle axes. For example, although the spectra of orthogonal radial modes often separate into two distinct series, one could intentionally overlap these series and create a balance point between two modes in which the addressed ions have strong mode participation, but this approach would increase the spectral density and reduce the robustness to frequency changes, as compared to well-separated radial series.

We also find that balance points exist between modes for which the ions have relatively large Lamb-Dicke parameters (i.e., mode participation). For long chains, a particular pair of ions can have relatively weak participation in a certain pair of modes, but there is always a pair of modes for which a balance point exists and ion participation remains strong. However, the pair of modes with the strongest ion participation is not guaranteed to be the lowest-frequency pair, and therefore the mode spacing (and robustness to frequency changes) can be less for these ions than for ion pairs that do participate strongly in the lowest two modes. We discuss the relationship between mode spacing and frequency robustness in greater detail in Sec. III D. Whether it is optimal to operate with weaker ion participation vs a smaller mode spacing depends on the exact mode spectra, level of motional frequency noise, and laser-power limitations.

### E. Gate comparison

To demonstrate the robustness to motional frequency changes of the balanced Gaussian gate, we simulate MS gates with three different gate designs subject to the symmetric frequency offset  $\delta\omega/2\pi$ , which corresponds to a common shift of each motional frequency:  $\nu'_k = \nu_k - \delta\omega$ , and we compute the contributions to the simulated state infidelity from displacement error  $\epsilon_d$  and from rotation-angle error  $\epsilon_r$  for each gate. We compare the balanced Gaussian gate, which has a detuning that solves Eq. (13), with an unbalanced Gaussian gate – which has a detuning that does not solve Eq. (13) – and with a square gate, which has a constant Rabi rate during the gate and the same detuning as the unbalanced Gaussian gate. In this comparison, both the unbalanced Gaussian gate and the square gate are detuned below the lowest motional mode. The duration of each gate is 250  $\mu\text{s}$  and the Gaussian width for each modulated gate is  $z = 33.1 \mu\text{s}$ . Being a small fraction of the gate duration, this choice of  $z$  creates Gaussian-like amplitude modulation with small truncation effects.

We provide a concrete example for this comparison by simulating each gate on the inner ions of a four-ion chain with an inner-ion separation of approximately 4.12  $\mu\text{m}$  and motional mode frequencies of  $\nu_{\text{rb}}/2\pi = \{2.14, 2.23, 2.30, 2.35\}$  MHz and  $\nu_{\text{ra}}/2\pi = \{2.39, 2.47, 2.53, 2.57\}$  MHz, in the orthogonal radial-b and radial-a directions, respectively. These motional frequencies are typical for a surface trap used in the QSCOUT device. In this order of modes (i.e., increasing energy), the Lamb-Dicke parameters for the two center ions ( $j_1 = 0$ ,  $j_2 = 1$ ) are,

$$\eta_{0,k_{\text{rb}}} = \{-6.27, 4.56, -1.91, 4.44\} \times 10^{-2}, \quad (14a)$$

$$\eta_{1,k_{\text{rb}}} = \{6.27, 4.56, 1.91, 4.44\} \times 10^{-2}, \quad (14b)$$

$$\eta_{0,k_{\text{ra}}} = \{-5.94, 4.33, -1.82, 4.24\} \times 10^{-2}, \quad (14c)$$

$$\eta_{1,k_{\text{ra}}} = \{5.94, 4.33, 1.82, 4.24\} \times 10^{-2}. \quad (14d)$$

We also assume the laser  $k$  vector is aligned at a  $45^\circ$  angle between the two radial directions, and we neglect any excitation of the axial motional modes, which will have a large detuning compared to the radial modes during the gate and are orthogonal to the  $k$  vector of the laser.

We choose to perform the balanced Gaussian gate by primarily targeting the lowest two radial modes. In this case, the lowest two modes are the  $k = 0$  and  $k = 1$  radial-b mode, which have a frequency spacing of  $\Delta\nu_{10}/2\pi = (\nu_1 - \nu_0)/2\pi = 88.5$  kHz. The targeted ions have Lamb-Dicke parameters that are equal and opposite in the  $k = 0$  mode, while being equal in the  $k = 1$  mode, such that the products  $\eta_{0,0}\eta_{1,0}$  and  $\eta_{0,1}\eta_{1,1}$  have opposite signs and are approximately equal in magnitude. We then solve Eq. (13) in the region between these modes and obtain a balanced detuning of  $\delta_0/2\pi = 51.2$  kHz above the  $k = 0$  mode. Also, because the sign of  $\theta$  happens to be negative in this case, we impose a differential laser phase of  $\pi$  between the two ions to achieve the gate defined by positive values of  $\theta$ . We model this change in phase by  $\sigma_{y,1} \rightarrow -\sigma_{y,1}$ , which modifies the handedness of the phase-space trajectories and has the same effect on the propagator  $U(\tau) = e^{-i\sigma_{y,0}\sigma_{y,1}\theta/2}$  as  $\theta \rightarrow -\theta$ .

In order to provide the most straightforward comparison of the balanced Gaussian gate to an unbalanced Gaussian gate and to a square gate, we use a similar magnitude of optimal detuning for all gates. For the unbalanced Gaussian and square gates, we choose a detuning of  $\delta_0/2\pi = -52$  kHz. We match the optimal detuning parameters in our comparison because the sensitivity to motional frequency changes strongly depends on the detuning from the nearest motional mode. For this reason, the rotation error of the unbalanced Gaussian gate has the same sensitivity to a symmetric detuning offset as the square gate in this example. We also note that this choice of  $\delta_0$  causes the ions to traverse  $n = \delta_0\tau/2\pi = 13$  phase-space loops during a

square gate, which corresponds to a relatively low sensitivity to frequency changes as compared to a single-loop gate with the same duration.

As a final step, we select the peak Rabi rate  $\Omega_0$  for each gate separately to guarantee  $|\theta| = \pi/2$  at the chosen detuning. The peak Rabi rates in our simulations of a four-ion chain are  $\Omega_0/2\pi = 130$  kHz for the square gate,  $\Omega_0/2\pi = 268$  kHz for the unbalanced Gaussian gate, and  $\Omega_0/2\pi = 178$  kHz for the balanced Gaussian gate. We have set the value of these peak Rabi rates to achieve the same target rotation angle  $\theta = \theta_{\text{target}} = \pi/2$  for each gate, at zero-frequency offset  $\delta\omega = 0$ . Given this constraint, the rotation-angle error  $\epsilon_r$  is proportional to  $|\theta_{\text{target}}|^2$  and does not explicitly depend on  $\Omega_0$ .

Figure 2 shows the simulated values of  $\epsilon_d$  and  $\epsilon_r$  for the three different gate designs as a function of the detuning  $\delta_0/2\pi$  from the  $k = 0$  mode. In this figure, each large peak in the errors corresponds to a detuning that is resonant with a motional mode, and as the detuning approaches each mode the errors are strongly dominated by contributions from that mode. As shown in Fig. 2(a), the Gaussian gates (dashed orange and solid blue) strongly suppress displacement error as long as the gates are performed sufficiently far from all motional modes. Truncating the Gaussian amplitude modulation leaves some small amount of abrupt turn-on and turn-off effects (i.e., square-gate character), giving rise to the sinlike oscillating floor. The height of the floor is set by the amount of truncation. Because  $z \ll \tau$  here, the truncation effect is small, and the floor of  $\epsilon_d$  is on the  $10^{-7}$  level. By contrast, the square gate (solid green) has narrow minima, and relatively high displacement error persists at all detunings in the range displayed.

Figure 2(b) shows the equivalent sensitivity of rotation error for the unbalanced Gaussian gate and for the square gate. In this figure, the dashed orange and solid green lines represent the rotation error of the unbalanced Gaussian and of the square gate, respectively, which are perfectly overlapped near their optimal detuning of  $\delta_0/2\pi = -52$  kHz. These gates have relatively narrow dips in rotation-angle error and thus have a small detuning range over which the target rotation angle of  $\theta = \pi/2$  is approximately achieved. By contrast, a broad dip in the rotation-angle error is apparent for the balanced Gaussian gate (solid blue) when  $d\theta/d\delta_c = 0$ . An intuitive explanation for this robustness against rotation error is that as the detuning moves in one direction away from the optimal point the contributions from some modes become smaller while the contributions from the other modes become larger.

To demonstrate the improved robustness to motional frequency changes when performing the balanced Gaussian gate, Fig. 3 shows the simulated state infidelity  $\epsilon_s$  for each gate design over a range of experimentally relevant symmetric detuning offsets  $\delta\omega/2\pi$ , which are defined relative to the optimal value of  $\delta_0/2\pi$  for each gate. This figure also shows the contributions to  $\epsilon_s$  from  $\epsilon_d$  and  $\epsilon_r$ , demonstrating

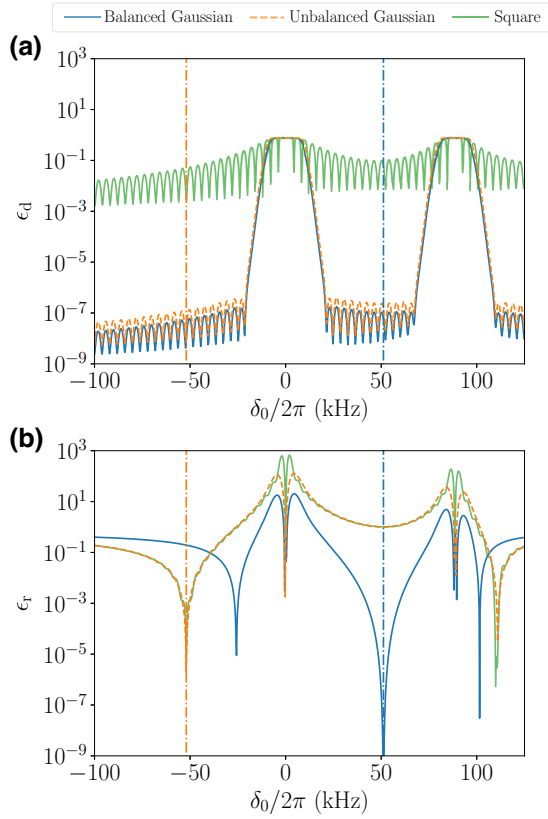


FIG. 2. (a) Displacement error  $\epsilon_d$  and (b) rotation-angle error  $\epsilon_r$  for a four-ion chain with three different gate designs. From bottom to top at most detunings, the curves correspond to a balanced Gaussian gate designed for a symmetric detuning of  $\delta_0/2\pi = 51.2$  kHz (solid blue), an unbalanced Gaussian gate designed for  $\delta_0/2\pi = -52$  kHz (dashed orange), and a square gate designed for  $\delta_0/2\pi = -52$  kHz (solid green). The detuning  $\delta_0 = 0$  is resonant with the lowest frequency motional mode, and the detuning  $\delta_0/2\pi = 88.5$  kHz is resonant with the second lowest motional mode, corresponding to the peaks in both error metrics. Vertical dash-dotted lines are drawn at  $\delta_0/2\pi = -52$  kHz (orange) and  $\delta_0/2\pi = 51.2$  kHz (blue).

that  $\epsilon_s$  is strongly dominated by  $\epsilon_r$  at small detuning offsets for the Gaussian gates, when  $\epsilon_s \gtrsim 10^{-7}$ . The vertical black dashed-dotted line at  $\delta\omega = 0$  indicates the optimal symmetric detuning for all gates, corresponding to both the blue and orange vertical lines in Fig. 2.

In this example, the distant modes have a nearly negligible effect on our design and simulations. The detunings from the motional modes are  $|\delta_0|/2\pi = 51.2$  kHz,  $|\delta_1|/2\pi = 37.3$  kHz,  $|\delta_2|/2\pi = 106$  kHz, and  $|\delta_3|/2\pi = 154$  kHz. Hence,  $|\delta_2/\delta_1| \approx 2.84$ , and the ion participation is smaller for mode  $k = 2$  than for mode  $k = 1$ ,  $|\eta_{0,2}\eta_{1,2}|/|\eta_{0,1}\eta_{1,1}| \approx 0.176$ . As a result,  $|\theta_2|$  is about 16 times smaller than  $|\theta_1|$ , and mode  $k = 2$  makes a small contribution to the rotation angle of the gate. Likewise, since  $|\delta_3/\delta_1| \approx 4.11$  and since mode  $k = 3$  has approximately the same ion participation as mode  $k = 1$ , we see that  $|\theta_3|$

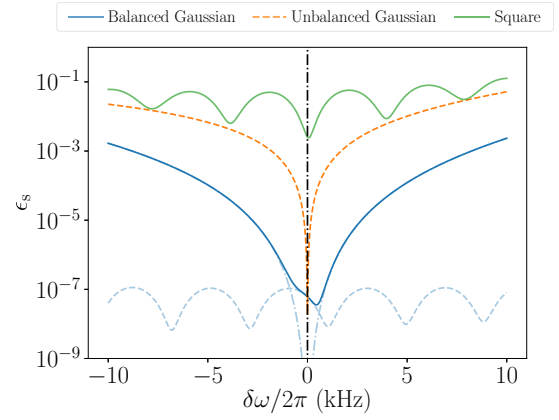


FIG. 3. The simulated state infidelity  $\epsilon_s = \epsilon_d + \epsilon_r$  for a four-ion chain with three different gate designs. The bold curves correspond to  $\epsilon_s$  for a balanced Gaussian gate (solid blue), an unbalanced Gaussian gate (dashed orange), and a square gate (solid green). The lighter curves correspond to the contributions  $\epsilon_d$  (dashed blue) and  $\epsilon_r$  (dashed-dotted blue) to  $\epsilon_s$ , showing that  $\epsilon_r$  dominates when  $\epsilon_s \gtrsim 10^{-7}$  for the Gaussian gates. The symmetric detuning offset  $\delta\omega/2\pi$  is defined relative to the optimal value of  $\delta_0/2\pi$  for each gate. The vertical black dashed-dotted line at  $\delta\omega = 0$  indicates the optimal symmetric detuning for all gates, corresponding to both the blue and orange vertical lines in Fig. 2.

is approximately 4 times smaller than  $|\theta_1|$ . However, this example also implies that distant modes can make a large contribution to the rotation angle if they have relatively large Lamb-Dicke parameters compared to the two closest modes.

### III. GATE IMPLEMENTATION

#### A. Gate parameter selection

In addition to choosing the correct detuning to balance the contributions of multiple motional modes, the width  $z$  of the truncated-Gaussian amplitude modulation is a free parameter that may be tuned to optimize the gate performance. This may be done numerically or empirically given sufficient intuition about the contributions to gate error. In particular, we find that optimal value of  $z$  for robustness to frequency changes depends on the detuning from the closest two motional modes. On the one hand, the truncation of the Gaussian modulation creates some square-gate character with an abrupt amplitude turn on. When  $z$  is much smaller than  $\tau$ , the truncation effect can be seen as the sinc-like oscillating floor in the plot of  $\epsilon_d$  in Fig. 2(a). Even though the truncation effect is small in this example, the contribution to  $\epsilon_d$  from the truncation effect can be large when the Gaussian width is comparable to the gate duration ( $z \approx \tau$ ). On the other hand,  $\epsilon_d$  can also be large when  $z$  is small enough such that  $e^{-\delta_k^2 z^2}$  is significant and fails to suppress the displacement error from mode  $k$ . This effect

can be understood as Fourier broadening of the amplitude modulation as the Gaussian shape becomes narrow in time. To optimize robustness, one can choose a value of  $z$  that balances the infidelity contribution from cutoff effects and Fourier broadening over a chosen range of frequency changes.

One must also take into consideration that as  $z$  is reduced, the peak intensity of the amplitude modulation can become an experimental challenge because the Rabi rate must be scaled up (by increasing  $\Omega_0$ ) to achieve the proper rotation angle of  $\theta = \pi/2$ . For Gaussian amplitude modulation, we find that the gate rotation angle  $\theta$  scales like  $z\Omega_0^2$ . As a result,  $\Omega_0$  must scale like  $1/\sqrt{z}$  to maintain a constant  $\theta$  as  $z$  changes. Likewise, since  $\theta_k \propto 1/\delta_k$ ,  $\Omega_0$  must scale like  $\sqrt{\delta_k}$  to maintain a constant  $\theta_k$  as  $\delta_k$  changes.

Additionally, the choice of modes targeted by the gate plays a role in its robustness to frequency changes. In general, a larger frequency spacing  $\Delta v_{k_2, k_1}/2\pi = (v_{k_2} - v_{k_1})/2\pi$  between motional modes  $k_1$  and  $k_2$  provides more robustness of both  $\epsilon_d$  and  $\epsilon_r$  to frequency changes. A larger frequency spacing allows for larger detunings ( $\delta_{k_1}$  and  $\delta_{k_2}$ ) through which  $\epsilon_d$  is strongly suppressed. Likewise, these larger detunings reduce the magnitude of  $d\theta/d\delta_c$  away from its zero crossing, reducing the sensitivity of  $\epsilon_r$  to frequency changes. For typical ion chains in a harmonic well, the lowest two modes have the largest frequency spacing and therefore the maximum robustness to frequency changes.

Because the gate parameters  $\delta_c$ ,  $z$ , and  $\Omega_0$  depend on the specific distribution of motional modes, we provide a concrete example of optimal parameter selection for the model of a four-ion chain described in Sec. II E, which targets the inner ions and the lowest two radial modes. To determine the optimal gate parameters and assess their robustness for this model, we numerically vary the Gaussian width  $z$  for a fixed gate duration of  $\tau = 250 \mu\text{s}$  and show the performance of the gate over a range of  $\delta\omega = \pm 10 \text{ kHz}$  in Fig. 4. At large values of  $z$  in this plot, the amplitude modulation is approximately constant during the gate, resembling a square gate and creating a strong truncation effect. In this regime, we recover an infidelity proportional to  $\text{sinc}(\delta\omega\tau)$ , as we expect for the Fourier transform of a constant amplitude. Toward the lower end of  $z$  on the plot, the amplitude modulation resembles a Gaussian with a small truncation effect, and we find that there is a broad region of  $z$  and  $\delta\omega$  where the gate performs well. For example, the simulated state infidelity  $\epsilon_s$  remains below  $10^{-3}$  over the range:  $-8.80 \text{ kHz} \leq \delta\omega/2\pi \leq 7.94 \text{ kHz}$  for  $z = 23.8 \mu\text{s}$  and over the range:  $12.3 \mu\text{s} \leq z \leq 61.5 \mu\text{s}$  for  $\delta\omega = 0$ .

In addition to Gaussian amplitude modulation, we have also simulated balanced MS gates with amplitude modulation of other spectrally compact shapes, including trapezoid amplitude modulation, and we found that the specific Gaussian shape was not necessarily better than other shapes whose Fourier transform falls off quickly with

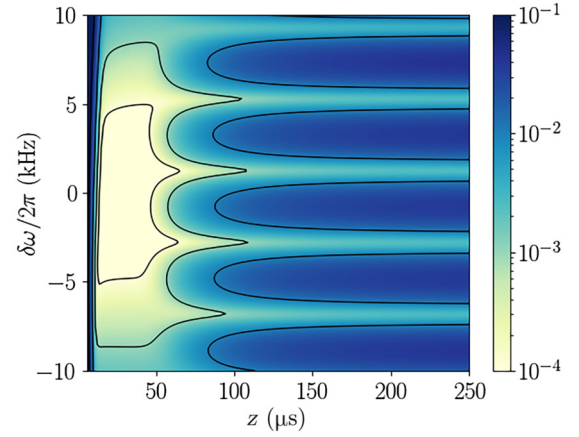


FIG. 4. Simulated state infidelity  $\epsilon_s$  as a function of the Gaussian width  $z$  and symmetric detuning offset  $\delta\omega$  for a truncated, balanced Gaussian MS gate on a four-ion chain. As the gate duration is  $\tau = 250 \mu\text{s}$ , the shape of amplitude modulation varies from a  $\delta$  function to a constant function, from left to right.

sideband detuning. As demonstrated by the set of Eq. (12), amplitude modulation can eliminate displacement error as long as the Fourier transform of the time-dependent Rabi rate evaluated at the detuning of each mode is sufficiently small (i.e., creates a displacement error that is smaller than all other errors). In the Gaussian case, Fig. 4 demonstrates the scale over which the Gaussian width can be modified without considerably affecting the robustness to frequency changes. Since the Fourier transform of a Gaussian amplitude decays exponentially with the square of the detuning, this region is broader and deeper than it would be for a trapezoid amplitude, e.g., but even a trapezoid amplitude could effectively eliminate displacement error for a sufficiently wide trapezoid or sparse motional mode spectra. Despite slightly increasing the displacement error for certain systems, one may still choose to use amplitude modulation with a higher ratio of pulse area to peak Rabi rate (like a trapezoid amplitude) to overcome experimental limitations in laser power or to decrease the gate duration for the same maximum laser power. In fact, within our balanced-gate scheme, one could develop more complicated amplitude shapes through numerical optimization to gain some other potential benefit, as long as the requirements on the Fourier transform of the amplitude that guarantee small displacement error are met.

While our system is limited by the maximum power of our 355-nm laser, other systems may not be as limited in laser power. We find that with only a modest increase in laser power, we could significantly decrease the duration  $\tau$  of our balanced Gaussian gate. Since reducing  $\tau$  while maintaining a fixed pulse area does not increase the sensitivity of rotation error to motional-frequency changes  $\delta\omega$ , we can maintain a fixed level of robustness (in the sum of rotation and displacement error) by increasing the

peak Rabi rate  $\Omega_0$  and decreasing the Gaussian width  $z$  to avoid significant cutoff effects from the shorter gate, until the displacement error due to Fourier broadening becomes dominant. In our simulations of the balanced Gaussian gate on the four-ion chain described above, we can decrease the gate duration to  $\tau = 50 \mu\text{s}$  and maintain a minimum fidelity of 98.7% over a  $\pm 10$  kHz range of  $\delta\omega$ . For this faster gate, we use  $z = 13 \mu\text{s}$  and  $\Omega_0/2\pi = 279$  kHz, which is only a factor of 1.59 times greater than the peak Rabi rate for  $\tau = 250 \mu\text{s}$  and  $z = 33.1 \mu\text{s}$ . While maintaining  $\delta\omega/2\pi = \pm 10$  kHz of robustness limits our gate duration to  $\tau \geq 50 \mu\text{s}$  in this case, this gate may be sufficiently fast if algorithmic runtimes are limited by other processes, like ion shuttling and recooling, for example.

Moreover, we could achieve faster gates by decreasing the ion separation to increase the frequency spacing between motional modes. This would allow for smaller Gaussian widths (or similar shapes) and even faster gates before the robustness is limited by Fourier broadening. However, even with less restrictive power limitations, crosstalk effects become relevant at small enough ion separations and require additional compensation techniques. Ultimately, given practical limitations in laser power and crosstalk effects, maintaining this large level of robustness within our gate design is likely limited to gate times on the order of  $10 \mu\text{s}$ . While even the  $50\text{-}\mu\text{s}$  gate duration would be significantly faster than the majority of two-qubit gates in state-of-the-art trapped-ion systems [12,36], much faster gates on trapped ions have been achieved using considerably different techniques [25].

## B. Experimental implementation

We implement the derived gate on a chain of  $N = 4$   $^{171}\text{Yb}^+$  ions to measure robustness to symmetric detuning offsets. We use the hyperfine ground, “clock” states as the qubit levels:  $|F = 0, m_F = 0\rangle \equiv |0\rangle$  and  $|F = 1, m_F = 0\rangle \equiv |1\rangle$ . In all experiments, all ions are initialized in  $|0\rangle$  and the gate under study is applied to two target ions. A global, single-qubit  $\pi/2$  rotation is then applied in parity scan measurements (described in Sec. III C). Finally, in all measurements, the population of each qubit state is determined by fluorescence detection, where population in state  $|i\rangle$  is revealed by the probability of detecting that state ( $\rho_i \approx P(i)$ ), up to a small measurement error. The relevant two-ion state is labeled as  $\text{Tr}_{c,d}(|a\rangle \otimes |b\rangle \otimes |c\rangle \otimes |d\rangle) \equiv |ab\rangle$  where  $a$  and  $b$  are the states of the two target ions;  $c$  and  $d$  are the states of the “spectator” ions in the chain, which are ignored.

We set the principal axes of the trap to be at a  $45^\circ$  angle from the effective Raman  $k$  vector to allow for Raman sideband cooling on all radial modes, and thus observe a total of  $2N$  radial motional frequencies. For the fidelity measurements presented here, we have radial motional frequencies of  $\nu_{\text{rb}}/2\pi = \{2.142, 2.230, 2.298, 2.347\}$  MHz

and  $\nu_{\text{ra}}/2\pi = \{2.388, 2.467, 2.528, 2.573\}$  MHz, and an axial center-of-mass frequency of  $\nu_{\text{axial, COM}}/2\pi = 0.45$  MHz. As modeled previously, we operate the gate between the lowest two radial modes.

The Gaussian amplitude modulation is approximated by a natural cubic spline with 13 amplitude knots that are passed to our custom Radio Frequency System-on-Chip (RFSoc) hardware, “Octet” [37]. Octet generates the rf waveforms that drive the acousto-optic modulators (AOMs), which perform the required RF to optical transduction. The spline knots are equally spaced along the square root of a Gaussian shape and applied to both the individual addressing beams and counterpropagating global beam AOMs, thus producing a Gaussian temporal profile in the two-photon Raman Rabi rate during the gate. The first and last knots of the spline are nonzero, and truncate parts of the infinite Gaussian lying outside of the gate duration.

We choose to implement a gate with  $z/\tau = 33.1 \mu\text{s}/250 \mu\text{s} \approx 0.13$  on the experiment to empirically minimize the effects of heating, truncation, and Fourier broadening while maintaining experimentally feasible Rabi rates (low enough to achieve both the balanced gate and an unbalanced gate at similar magnitude detuning for fair comparison). The balance-point detuning  $\delta_c$ , as defined by Eq. (13), is found by scanning the symmetric detuning and finding the point of zero slope in the  $|11\rangle$  population, and the peak Rabi rate  $\Omega_0$  is set by varying the scaling of the Gaussian amplitude modulation and finding the point of equal  $|00\rangle$  and  $|11\rangle$  populations. For the balanced Gaussian gate demonstrated here on the center pair of ions,  $\delta_0/2\pi = 52$  kHz (where  $\delta_0 = \delta_c - \nu_0$ ) and  $\Omega_0/2\pi \approx 180$  kHz.

We emphasize that these calibrations are fast and straightforward to implement in hardware, imposing low calibration overhead compared to numerically solved optimal waveform alternatives with many parameters. In addition, because we only require that the laser waveform has a spectrally compact Fourier transform, there is no need to account for small differences in the designed and experimentally produced waveforms. This is particularly beneficial in the case of AOM-driven waveform shaping, where the diffraction efficiency is frequency dependent and nonlinear in rf power when operated near peak efficiency. Therefore, our method avoids much of the painstaking calibrations of AOM frequency and power response that are often required for other numerically optimized waveforms.

Although the wavelength (355 nm) of the Raman laser is chosen to approximately balance the ac Stark shift on the qubit transition, there remains a residual differential ac Stark shift on the order of 1 kHz. To compensate for this shift, we dynamically apply a virtual frame rotation at a rate proportional to the intensity of the laser applied to each ion. The magnitude of the frame rotation is found by

preparing in the  $|00\rangle$  state, applying two MS gates back to back, and maximizing the resultant population in the  $|11\rangle$  state.

### C. Experimental results

We measure the performance of the balanced Gaussian MS gate and compare it to the unbalanced Gaussian and square MS gates. While out-of-model technical noise appears to limit the fidelity of the balanced gate, there is a clear difference in the response to intentionally applied symmetric detuning offsets for each gate. At several points in the measured range of detuning offsets, we measure both the even parity population after an MS gate on its own and the parity contrast resulting from a single-qubit  $\pi/2$  gate with variable phase on both ions following the MS gate. We then estimate the fidelity ( $\mathcal{F}$ ) according to [41–44],

$$\mathcal{F} = \frac{1}{2}(\rho_{00} + \rho_{11}) + \frac{1}{2}A_\pi, \quad (15)$$

where  $\rho_{ab}$  is the population of the  $|ab\rangle$  state after the MS gate and  $A_\pi$  is the measured contrast of a parity oscillation.

We apply the gates to the inner two ions in a four-ion chain, operating between the  $k = 0$  and  $k = 1$  modes, and we present the gate performance in Fig. 5. In a scan of the symmetric detuning offset, we prepare the ions in  $|00\rangle$ ; the gate is applied; and the populations are read out. The even-parity populations serve as an indicator for gate angle and show that the correct gate angle is achieved in a range of approximately  $\pm 10$  kHz centered around  $\delta_0/2\pi = 52$  kHz relative to the  $k = 0$  mode, when  $\rho_{00} \approx 0.5 \approx \rho_{11}$ . The odd-parity population ( $\rho_{01} + \rho_{10}$ ) is an indicator of displacement error, and shows good performance (population is near zero) as long as the detuning is sufficiently far from the motional modes.

We then estimate the fidelity of the gate at various symmetric detuning offsets by taking both a parity measurement with 2000 shots at both the top and bottom of a parity curve ( $\pi/4$  and  $3\pi/4$  phase offset between the MS gate and subsequent single-qubit  $\pi/2$  gate) and a population measurement with 4000 shots at each detuning. We find that the infidelity of the balanced Gaussian MS gate increases by  $< 1\%$  over  $\delta\omega/2\pi \leq \pm 10$  kHz, indicating broad robustness to symmetric detuning offset. In this range, the infidelity experiences a flat noise floor, over which all data points are within uncertainty of each other. As all other gate designs in the literature demonstrate a  $< 1\%$  infidelity increase over a range of  $\lesssim \pm 1$  kHz, our demonstration represents an order-of-magnitude improvement in the robustness to frequency changes. The square gate shown here has the same gate duration and (approximate) detuning as the Gaussian gates, causing the ions to traverse 13 loops in phase space during the gate. We find this gate to be a more fair comparison than a single-loop square gate because using the same detuning and duration

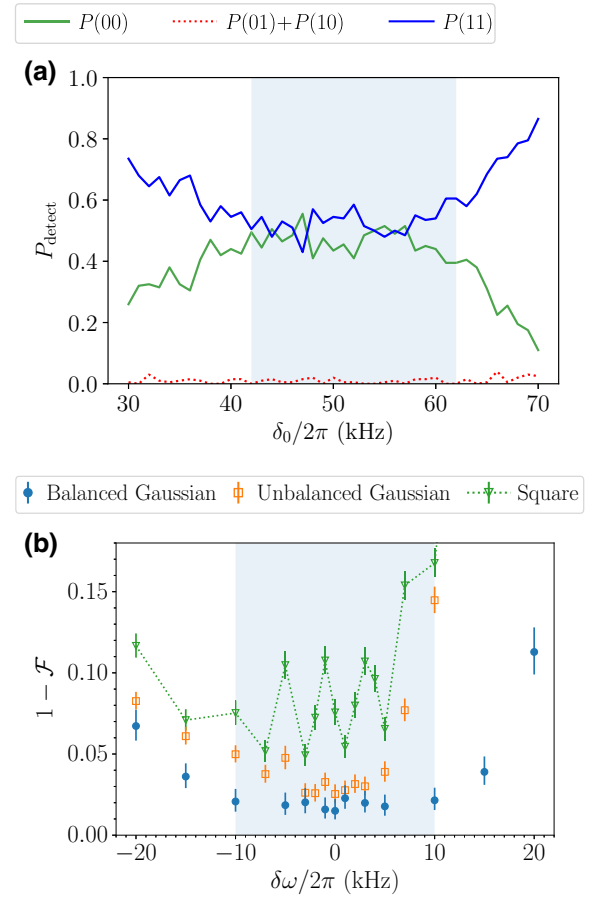


FIG. 5. Balanced Gaussian gate performance measurements. (a) A symmetric detuning scan between two motional modes (nearest modes are at 0 kHz and approximately 88.5 kHz) shows a broad region around  $\delta_0/2\pi = 52$  kHz where the balanced Gaussian gate performs well (shaded region). Lines top to bottom at  $\delta_0/2\pi = 30$  kHz are the detection probabilities  $P(11)$  (solid blue),  $P(00)$  (solid green), and  $P(01) + P(10)$  (dotted red) after preparing in  $|00\rangle$  and applying the gate. (b) Measured entangling gate infidelity ( $1 - \mathcal{F}$ ) as a function of symmetric detuning offset for the square (triangles), unbalanced Gaussian (squares), and balanced Gaussian (circles) gates. Lines for the square gate are a guide to the eye. The fidelity ( $\mathcal{F}$ ) is calculated according to Eq. (15) using the parity scan results and population measurements. Uncertainties markers are 95% confidence intervals numerically calculated by assuming a binomial distribution for each measurement.

produces a more similar interaction strength and maximum displacement during the gate.

We also use the population measurements to calculate the gate angle according to  $\theta = \arcsin[\rho_{11}/(1 - (\rho_{01} + \rho_{10}))]$ . For the balanced Gaussian gate, we find that there is a clear cancellation of first-order gate-angle dependence on the symmetric detuning [see Fig. 6(a)] and a corresponding insensitivity to rotation error [see Fig. 6(b)]. By contrast, for the comparable unbalanced Gaussian gate using the same magnitude detuning from the

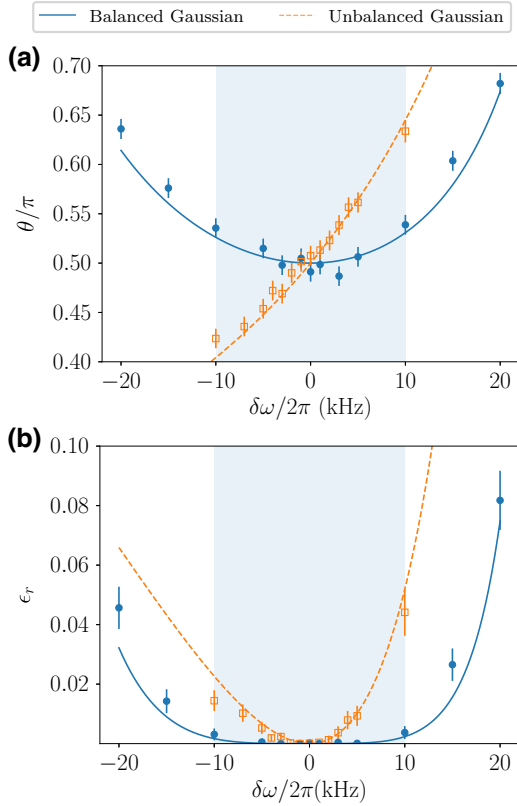


FIG. 6. (a) Measured (points) and calculated (lines) rotation angle as a function of symmetric detuning offset ( $\delta\omega$ ) for both the balanced (solid blue) and unbalanced (dashed orange) Gaussian gates shows the cancellation of first-order dependence of rotation angle on detuning near the balance point. Target rotation angle is  $\pi/2$ . (b) Measured rotation error as calculated by the approximate form of Eq. (10). Uncertainty markers are derived by propagating Wilson score intervals from population measurements through all calculations. The theory curves, which have no free parameters, show good agreement with the experimental data.

lowest radial mode with the opposite sign ( $\delta_0/2\pi = -52$  kHz), we instead see an approximately linear dependence of gate rotation angle on symmetric detuning. Since the unbalanced gate predominantly uses only one mode, it also requires increasing the laser power to achieve  $\theta = \pi/2$ .

We note that the peak fidelity of our experimental implementation of the balanced Gaussian gate is only  $98.5^{+0.5}_{-0.7}\%$ . We contribute the cause of the approximately 1.5% infidelity floor to technical noise that is not included in our theoretical model. For the purpose of this article, the good agreement between theory and experiment in our measurement of  $\theta$  and  $\epsilon_r$  as a functions of symmetric detuning offset in Fig. 6 demonstrates the robustness of our gate design to this single error source. Given this agreement, the demonstrated robustness should remain for high-fidelity experimental implementations of the balanced Gaussian gate as well. We will provide estimates of

TABLE I. Empirically determined balanced Gaussian gate detuning ( $\delta_k$ , relative to mode index  $k$ ) and performance for all six pairs of ions in a four-ion chain. Ions indices ( $j_1, j_2$ ) from left to right in the chain are  $\{-1, 0, 1, 2\}$ .  $\Delta\epsilon_{s,\max}(\%)$  is the maximum decrease in fidelity at  $\delta\omega/2\pi = \pm 3$  kHz compared to at the fidelity ( $\mathcal{F}_0$ ) at the calibrated detuning ( $\delta_k$ ).

$j_1$	$j_2$	$k$	$\delta_k/2\pi$ (kHz)	$\mathcal{F}_0$ (%)	$\Delta\epsilon_{s,\max}(\%)$
0	1	0	52	$98.7^{+0.3}_{-0.3}$	0.4
0	-1	1	42	$98.1^{+0.4}_{-0.4}$	0.4
1	-1	0	37	$98.4^{+0.4}_{-0.4}$	0.5
0	2	0	37	$97.5^{+0.4}_{-0.5}$	0.6
1	2	1	37	$98.0^{+0.4}_{-0.4}$	0.4
-1	2	1	30	$98.0^{+0.4}_{-0.4}$	0.5

the fidelity impact due to small motional frequency errors through simulations of high-fidelity balanced Gaussian gates in Sec. III D.

To demonstrate the generality of our design, we empirically calibrate a balanced Gaussian gate on all six pairs of ions in a four-ion chain. For this data,  $\tau = 125 \mu\text{s}$  gate time is used to slightly improve gate performance, while  $250 \mu\text{s}$  was used for the Fig. 5 data to allow for a sufficiently low Rabi rate to perform the unbalanced comparison gate. In all cases,  $z/\tau$  is held constant. For each pair, we scan the symmetric detuning offset and find detunings where the rotation angle is flat with respect to frequency and the interaction strength is relatively large (i.e., a low laser power is required). The resulting operating detunings relative to mode  $k$  are listed in Table I. We then scan the Rabi rate to achieve  $\theta = \pi/2$  and compensate for the ac Stark shift as described in Sec. III B. These calibrations are fast (roughly 2 min per pair) and require no *a priori* calculations. Because our gate design is robust to small changes in motional spectra, we also note that we could further expedite recalibrations by scanning over a smaller range of symmetric detuning and peak Rabi rate. Finally, we perform a ‘‘spot check’’ of the robustness of each of these gates against motional frequency error by measuring the maximum increase in infidelity ( $\epsilon_{s,\max}$ ) at  $\delta\omega/2\pi = \pm 3$  kHz and find  $\epsilon_{s,\max} < 1\%$  in all cases.

#### D. Extension to larger numbers of ions

We extend our numerical simulations to explore the performance of the balanced Gaussian gate on ion chains of variable length from  $N = 2$  up to  $N = 33$ . While our simple model leaves out many experimental details important to long chains, we still expect our simulations to accurately estimate the impact of motional frequency changes on MS-gate performance, including the effects from an increased density of motional spectra. In addition, we expect our simulations to provide accurate estimates of the peak Rabi rate required to perform our gate on long ion chains.

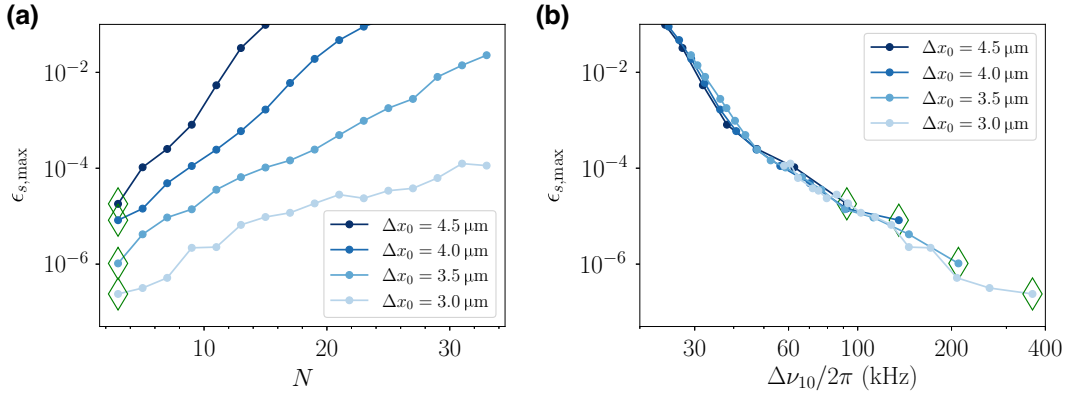


FIG. 7. The sensitivity to frequency changes, as quantified by the maximum state infidelity  $\epsilon_{s,\max}$  over a range of  $\pm 3$  kHz from the minimum of  $\epsilon_s$  vs  $\delta\omega$  for odd  $N$  from 3 to 33. The motional frequency spacing  $\Delta\nu_{10}/2\pi$  decreases monotonically with increasing  $N$ . From light to dark in each plot, the ion separation is  $\Delta x_0 = 3 \mu\text{m}$  to  $4.5 \mu\text{m}$  in steps of  $0.5 \mu\text{m}$ . The green diamonds indicate  $N = 3$  for each ion separation. These plots show that the balanced Gaussian gate can remain robust to frequency changes as the chain length grows and that  $\Delta\nu_{10}$  is a good predictor of the sensitivity to motional frequency changes for the range of parameters considered in this work. The Appendix discusses these simulations for even  $N$ .

As described in Sec. III A, we choose to target the lowest two motional modes ( $k = 0$  and  $k = 1$ ) of the  $N$ -ion chain because we expect to achieve more robustness to motional frequency changes by targeting the neighboring modes with the largest frequency spacing. In the region between these modes, we find a detuning  $\delta_c$  that solves Eq. (13) and balances the contributions to  $\theta$  from all modes, which is possible when the products  $\eta_{j_1,0}\eta_{j_2,0}$  and  $\eta_{j_1,1}\eta_{j_2,1}$  have opposite signs. Our simulations in this section also include all modes, but similar to our four-ion example discussed above, the contributions from the nearest two modes dominate both  $\epsilon_d$  and  $\epsilon_r$  in these simulations.

To maintain consistency in the sign and magnitude of the Lamb-Dicke parameters between chains of different  $N$ , we target the ions to the immediate left and right of center, for which we find a solution to Eq. (13) in each case. The targeted ions are the two center ions of the chain for even  $N$  and the two ions next to the center ion for odd  $N$ . For this choice of ions, targeting the lowest two modes leads to a balanced gate with a value of  $\delta_c$  that solves Eq. (13); however,  $\theta$  has the opposite sign for even  $N$  versus odd  $N$ . To maintain the same target gate in our simulations for both even and odd  $N$ , we impose a differential laser phase of  $\pi$  between the two ions for even  $N$ , as we did in the four-ion example, and we set this phase to zero for odd  $N$ .

As  $N$  grows, we relax the strength of a harmonic potential in the axial direction such that, for all  $N$ , the separation between the equilibrium positions of the two center ions (the center ion and its neighbors) for even (odd)  $N$  is a fixed value,  $\Delta x_0$ . We make this choice to maintain consistency with an experimental apparatus designed for a fixed individual addressing beam separation. At the same time, we keep the strength of harmonic potentials in the radial

directions fixed as we increase  $N$ , maintaining consistent center-of-mass frequencies in the radial directions. As a result, the radial sideband spectrum becomes increasingly dense as  $N$  grows because the spacing of radial modes is set by the ratio of the axial to radial confinement. While we will refer to  $\Delta x_0$  as the ion separation, we note that the precise separation of each neighboring pair of ions will increase from the center to the edge of the chain for any particular  $N$ , as we model a simple harmonic potential in the axial direction. The use of anharmonic potentials to keep the ion spacing constant within a chain has been considered in other works [45–47], but we deem the implementation of a nonharmonic potential to be outside the scope of this investigation.

In this section, we use the same waveform parameters as in our main four-ion example:  $\tau = 250 \mu\text{s}$  and  $z = 33.1 \mu\text{s}$  for each  $N$  and  $\Delta x_0$ . However, for the radial center-of-mass frequencies in our experiment, the series of radial-a and radial-b modes would overlap for the small values of  $\Delta x_0$  and small  $N$  that we explore in this section. Although one can implement balanced Gaussian gates with overlapping spectral series, for simplicity, we slightly decrease the radial-b motional frequencies to ensure that the two radial series do not overlap for all  $N$  and  $\Delta x_0$  explored in this section. Here, we use  $\nu_{N-1}/2\pi = 2.24$  MHz and  $\nu_{2N-1}/2\pi = 2.57$  MHz for the radial center-of-mass frequencies.

While our simulations indicate that the balanced MS gates have similar performance on chains of even and odd  $N$ , slight differences in ion participation in the lowest two modes cause our simulated infidelity for even  $N$  to be slightly worse than for odd  $N$  of a similar magnitude. In order to simplify our discussion of the sensitivity to frequency changes as a function of  $N$ , we choose to focus

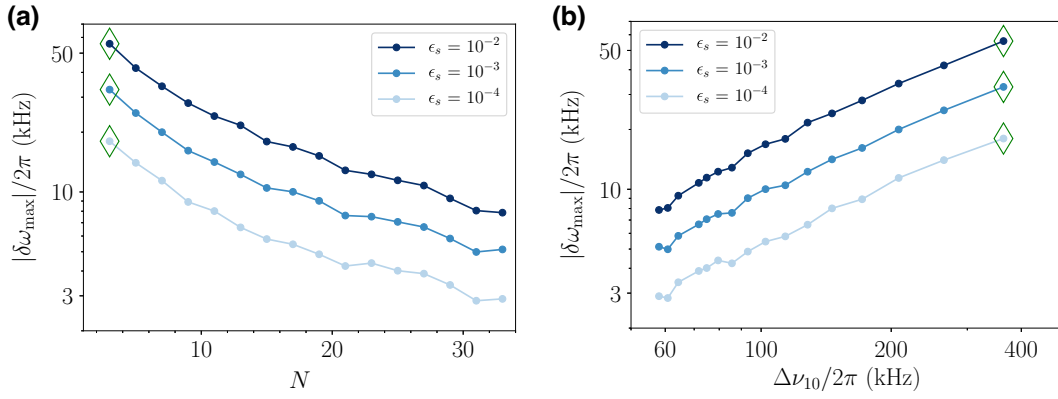


FIG. 8. The sensitivity to frequency changes, as quantified by the bandwidth  $\delta\omega_{\max}$  for which a minimum state infidelity of  $\epsilon_s$  is maintained, for odd  $N$  from 3 to 33 with  $\Delta x_0 = 3 \mu\text{m}$ . The bandwidth is measured relative to the minimum of  $\epsilon_s$  vs  $\delta\omega$ , and is displayed separately for increasing values of the minimum  $\epsilon_s$  from light to dark. The motional frequency spacing  $\Delta\nu_{10}/2\pi$  decreases monotonically with increasing  $N$ . The green diamonds indicate  $N = 3$  for each  $\epsilon_s$ . The Appendix discusses these simulations for even  $N$ .

on our simulations for odd  $N$  in this section. We discuss our simulations for even  $N$  and how they differ from our simulations for odd  $N$  in the Appendix.

To quantify the sensitivity to motional frequency changes for each  $N$ , we compute the maximum state infidelity  $\epsilon_{s,\max}$  over a  $\pm 3$  kHz range from the symmetric detuning offset that minimizes  $\epsilon_s$ . Figure 7 shows this measure of sensitivity for odd  $N$  and for an ion separation of  $\Delta x_0 = 3 \mu\text{m}$  to  $4.5 \mu\text{m}$ . The same values of  $\epsilon_{s,\max}$  are plotted vs  $N$  and vs  $\Delta\nu_{10}/2\pi$ , the frequency spacing between the lowest two motional modes. The green diamonds indicate  $N = 3$  for each ion separation. From Fig. 7, we see that  $\epsilon_{s,\max}$  exceeds  $10^{-2}$  around  $N = 11$  for  $\Delta x_0 = 4.5 \mu\text{m}$ , and we see that this measure of sensitivity decreases dramatically with decreasing  $\Delta x_0$ , allowing  $\epsilon_{s,\max}$  to remain below  $10^{-4}$  for all (odd)  $N$  in this study when  $\Delta x_0 = 3 \mu\text{m}$ .

As shown in Fig. 7(b),  $\epsilon_{s,\max}$  is approximately a function of only the frequency spacing between the lowest two modes  $\Delta\nu_{10}/2\pi$  for each ion separation, despite the different motional frequencies, Lamb-Dicke parameters, number of ions  $N$ , and waveform parameters  $\delta_c$  and  $\Omega_0$ . Note that the value of  $\Delta\nu_{10}$  decreases with larger  $N$  (for fixed ion separation) and increases for smaller ion separation (at fixed  $N$ ), shifting the plots vs  $\Delta\nu_{10}/2\pi$  to the left for increasing ion separation. Since  $\Delta\nu_{10}$  appears to be a good predictor of balanced Gaussian gate performance in these simulations, we note that designs of new experiments intending to implement these gates should consider the mode spacing when choosing an ion separation and chain length.

The approximate correspondence between  $\epsilon_{s,\max}$  and  $\Delta\nu_{10}$  arises because  $\epsilon_s$  is dominated by the contribution from  $\epsilon_r$  for the chains we have considered. When  $\epsilon_d$  makes a significant contribution to  $\epsilon_s$ ,  $\Delta\nu_{10}$  becomes a worse

predictor of gate performance. In our simulations, this situation arises for even  $N$  and small  $\Delta\nu_{10}$  (large  $N$ ). We show the contributions of  $\epsilon_d$  and  $\epsilon_r$  to  $\epsilon_s$  and discuss the breakdown of the  $\Delta\nu_{10}$  predictor in the Appendix.

While we do not have experimental verification of the robustness of our gate design for fidelities higher than  $\mathcal{F} = 98.5\%$ , our simulations predict the bandwidth of  $\delta\omega$  over which higher fidelities can be maintained. Figure 8 shows the predicted bandwidth for an ion separation of  $\Delta x_0 = 3 \mu\text{m}$ , where the total state infidelity is approximately equal to  $\epsilon_s = \epsilon_r + \epsilon_d$ . As this figure includes a large bandwidth for high-fidelity gates, including relatively long chain lengths, these results indicate that our gate design may be useful in future devices with much higher fidelities than achieved in our proof-of-principle experiment. For example, our simulations predict a state fidelity of  $\mathcal{F} \geq 99.99\%$  for all odd  $N$  in our study with a bandwidth requirement of only  $\delta\omega/2\pi \lesssim \pm 3$  kHz.

For the simulations presented in Fig. 8, we have reduced the ion separation to  $\Delta x_0 = 3 \mu\text{m}$  to increase  $\Delta\nu_{10}$  and improve the performance of MS gates at experimentally relevant frequency changes for large  $N$ . Although this improves the robustness of our simulated gates, a reduction in  $\Delta x_0$  could have detrimental effects on quantum circuit performance that are not included in our simulations by, for example, increasing the level of crosstalk between neighboring qubits [48]. While we do not explicitly include crosstalk in our simulations, an ion separation of  $\Delta x_0 = 3 \mu\text{m}$  remains experimentally relevant in modern trapped-ion devices. In addition, even smaller ion separations remain an interesting avenue for future research, as there has been promising research on applying spin-echo pulses to cancel out the effects of crosstalk when individual ions cannot be perfectly resolved [49]. Alternatively, one could decrease the radial motional frequencies to increase

$\Delta\nu_{10}$ , but one needs to balance this increased robustness to frequency changes with the additional amount of anomalous heating experienced by lower frequency motional modes.

The relatively large range of frequency changes explored in this paper is set by the frequency spacing of the radial modes in our four-ion experiments. As shown in Figs. 7 and 8, reducing the frequency spacing comes at the expense of some robustness, but at the same time, a reduction in the frequency spacing can significantly reduce power requirements. As the contribution to gate rotation angle  $\theta$  from mode  $k$  scales like  $\theta_k \propto \Omega_0^2/\delta_k$  for  $\delta_k \gg z^{-1}$ , the optical power ( $\propto \Omega_0^2$ ) may be reduced approximately linearly with detuning (set by the mode spacing) to maintain constant  $\theta$ . In practice, one can engineer the frequency spacing to achieve the desired parameters in the power-robustness trade space by, for example, adjusting the ratio of the axial to radial confinement.

Depending on the ion pair used in the gate, targeting the lowest two modes requires increasingly challenging laser powers as the length of the chain increases, due to poor ion participation in these modes. However, one can reduce power requirements by targeting modes with relatively strong  $\eta_{i,k}$  for those ions. The laser-power requirement is further reduced due to the smaller frequency spacing between modes, at the expense of some robustness. For example, a chain of length  $N = 5$  with an ion separation of  $\Delta x_0 = 4.12 \mu\text{m}$  (approximately corresponding to the ion separation in our experiments) has a lowest-mode frequency spacing of  $\Delta\nu_{10}/2\pi = 83.5 \text{ kHz}$ . When targeting the outermost ions and the lowest two modes in this chain, the balanced Gaussian gate has detuning from the lowest mode of  $\delta_0/2\pi = 36.3 \text{ kHz}$  and requires a max Rabi rate of  $\Omega_0/2\pi = 665 \text{ kHz}$ . We can reduce this requirement by addressing the  $k = 2$  and  $k = 3$  radial modes as the main contributors to the balanced Gaussian gate, which have comparable  $\eta_{i,k}$  to the next-to-center ions in the lowest two modes. The balanced detuning for this gate is  $\delta_2/2\pi = 24.6 \text{ kHz}$ , and the frequency spacing between the nearest two modes is  $\Delta\nu_{32}/2\pi = 52.4 \text{ kHz}$ , leading to strong robustness to frequency changes. Yet, this gate requires only  $\Omega_0/2\pi = 148 \text{ kHz}$ , which is less than the peak Rabi rate of  $\Omega_0/2\pi = 185 \text{ kHz}$  required to perform the balanced gate between these two modes on the next-to-center ions.

For longer ion chains, we still expect the fast and simple calibration routine for our gate design to benefit these systems. Because some ion-participation factors decrease for longer ion chains, which can lead to large laser-power requirements, one may want to target different modes for each pair of ions. While this strategy slightly complicates the calibration routine, as compared to targeting the same modes for each ion pair, the calibration time should be the same for each strategy. In addition, while larger ion chains may suffer from irregular drift in the motional spectra,

the optimal parameters for our gate design (symmetric detuning offset and peak Rabi rate) remain robust to small—but arbitrary—changes in motional spectra.

#### IV. CONCLUSION AND OUTLOOK

In summary, we have designed an MS gate that is strongly robust to motional frequency changes, addressing a key error source in trapped-ion entangling gates that limits the scalability of both QCCD and longer-chain architectures. Our design employs a class of spectrally compact laser waveforms that strongly suppress coherent displacement errors. These waveforms also have a specific, constant laser frequency that balances the contributions to rotation angle from all motional modes, generating a broad robustness to rotation-angle errors. Further, these waveforms have a simple parameterization that removes the need to optimize a large set of waveform parameters, providing low computational overhead and technical complexity.

Our proof-of-concept implementation of this gate design on a four-ion chain maintained a  $<1\%$  reduction from the peak fidelity over a  $\pm 10 \text{ kHz}$  range of an applied frequency offset (used to mimic motional-frequency changes), an order-of-magnitude improvement over state-of-the-art techniques. Our numerical simulations of the gate design predict that a high-level of robustness can be maintained for longer ion chains. Additionally, the combination the robustness and the low technical complexity of our design suggests a dramatic benefit for QCCD architectures, where efficient, long-lasting calibration is pivotal for scaling to larger numbers of ions and for performing longer quantum algorithms. Finally, the simplicity of our gate design allows the immediate adoption of our technique on contemporary trapped-ion systems. Together, these features promise that our gate design will be valuable for accelerating the development of next-generation quantum computing architectures.

#### ACKNOWLEDGMENTS

We thank Kenneth R. Brown for illuminating discussions.

This research was supported by the U.S. Department of Energy, Office of Science, Office of Advanced Scientific Computing Research Quantum Testbed Program. Sandia National Laboratories is a multimission laboratory managed and operated by National Technology & Engineering Solutions of Sandia, LLC, a wholly owned subsidiary of Honeywell International Inc., for the U.S. Department of Energy's National Nuclear Security Administration under Contract No. DE-NA0003525.

B.P.R. and M.N.H.C. contributed equally to this work.

This article describes objective technical results and analysis. Any subjective views or opinions that might

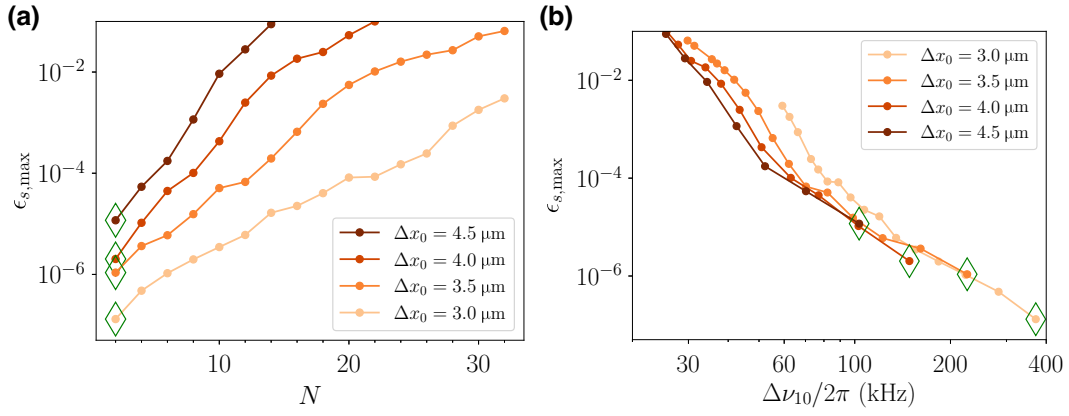


FIG. 9. The sensitivity to frequency changes, as quantified by the maximum state infidelity  $\epsilon_{s,\max}$  over a range of  $\pm 3$  kHz from the minimum of  $\epsilon_s$  vs  $\delta\omega$  for even  $N$  from 2 to 32. The motional frequency spacing  $\Delta\nu_{10}/2\pi$  decreases monotonically with increasing  $N$ . From light to dark in each plot, the ion separation is  $\Delta x_0 = 3 \mu\text{m}$  to  $4.5 \mu\text{m}$  in steps of  $0.5 \mu\text{m}$ . The green diamonds indicate  $N = 2$  for each ion separation. These plots show a similar but slightly worse robustness to frequency changes, as compared to these same plots for odd  $N$  in Sec. III D. We also see that  $\Delta\nu_{10}$  is a worse predictor of the sensitivity to motional frequency changes for even  $N$ , as compared to odd  $N$ , due to the larger contribution to  $\epsilon_s$  from  $\epsilon_d$  for even  $N$ .

be expressed in the article do not necessarily represent the views of the U.S. Department of Energy or the U.S. Government.

#### APPENDIX: SIMULATIONS OF A BALANCED GAUSSIAN MS GATE FOR EVEN $N$

Here, we discuss our simulations of the balanced Gaussian gate for chain lengths of even  $N$ , and we explore when  $\Delta\nu_{10}$  breaks down as a good predictor of motional frequency robustness. Using the same model parameters as in Sec. III D, Figs. 9 and 10 show a similar but slightly worse performance of the balanced MS gate for even  $N$ , as compared to the simulations for odd  $N$  of a similar

magnitude shown in Sec. III D. We also see that  $\Delta\nu_{10}$  becomes a worse predictor of gate performance for large  $N$  and small  $\Delta\nu_{10}$ . For example, Fig. 9(b) shows that, for small  $\Delta\nu_{10}$ , a relatively small ion separation of  $\Delta x_0 = 3 \mu\text{m}$  (lightest curve) has an increased value of  $\epsilon_{s,\max}$  compared to chains with larger ion separations (darker curves) for similar values of  $\Delta\nu_{10}$ . Likewise, Fig. 10(b) shows that the bandwidth  $|\delta\omega_{\max}|$  has a stronger dependence on  $\Delta\nu_{10}$  at small  $\Delta\nu_{10}$  (large  $N$ ) than for odd  $N$ .

This slight reduction in the robustness for even  $N$  arises because the Lamb-Dicke parameters of the lowest two modes for each chain cause the value of  $\delta_c$  that solves Eq. (13) to lie much closer to the  $k = 1$  mode for even  $N$  than for similar values of odd  $N$ , leading to a larger

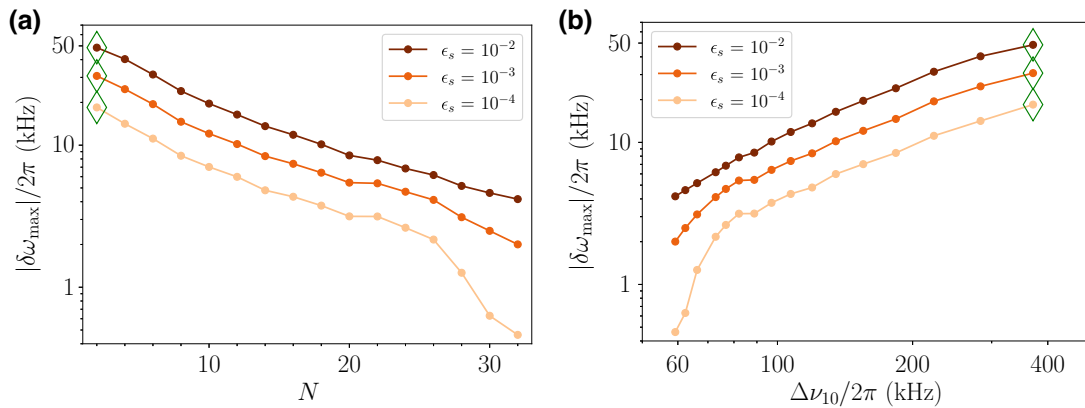


FIG. 10. The sensitivity to frequency changes, as quantified by the bandwidth  $\delta\omega_{\max}$  for which a minimum state infidelity of  $\epsilon_s$  is maintained, for even  $N$  from 2 to 32 with  $\Delta x_0 = 3 \mu\text{m}$ . The bandwidth is measured relative to the minimum of  $\epsilon_s$  vs  $\delta\omega$ , and is displayed separately for increasing values of the minimum  $\epsilon_s$  from light to dark. The motional frequency spacing  $\Delta\nu_{10}/2\pi$  decreases monotonically with increasing  $N$ . The green diamonds indicate  $N = 2$  for each  $\epsilon_s$ . These plots show a similar but slightly worse robustness to frequency changes, as compared to these same plots for odd  $N$  in Sec. III D.

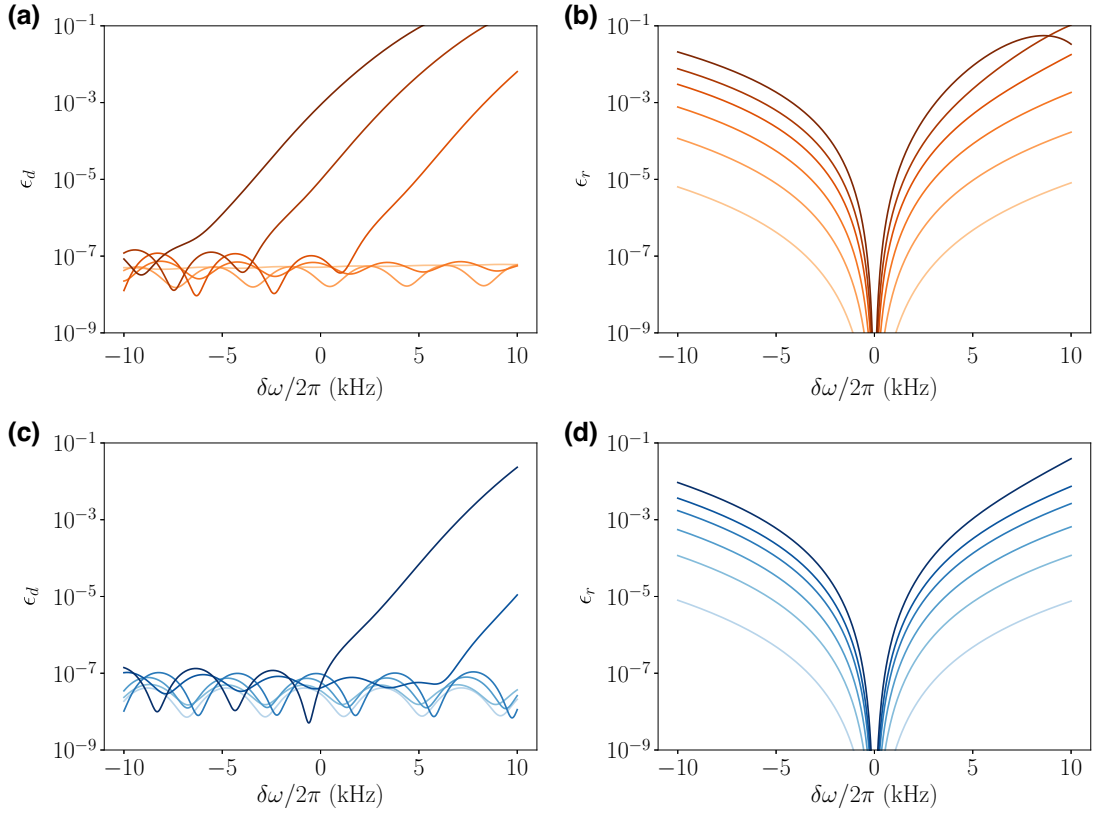


FIG. 11. (a),(c) The simulated displacement error  $\epsilon_d$  and (b),(d) the simulated rotation-angle error  $\epsilon_r$  vs the symmetric detuning offset  $\delta\omega$  for an ion separation of  $\Delta x_0 = 3.0 \mu\text{m}$ . The curves correspond to (a),(b) even  $N$  from 2 to 32 and to (c),(d) odd  $N$  from 3 to 33, from light to dark in steps of 6. For most  $N$  shown here,  $\epsilon_r$  dominates as the main limiting factor for gate robustness to motional frequency changes. For larger  $N$ ,  $\epsilon_d$  eventually lifts off the Gaussian truncation floor as the motional modes bunch closer together and significantly reduce error suppression from the factor of  $e^{-\delta_k^2 z^2}$  in Eq. (12b).

contribution from  $\epsilon_d$  and a higher sensitivity to frequency changes for even  $N$ . Moreover, the approximate correspondence between  $\epsilon_{s,\text{max}}$  and  $\Delta\nu_{10}$  arises when  $\epsilon_r$  is the dominant contribution to  $\epsilon_s$ . When  $\epsilon_r$  strongly dominates  $\epsilon_d$ , the sensitivity depends only on the magnitude of  $d^2\theta/d\delta\omega^2$  at  $\delta\omega = 0$ , which is set by  $\Delta\nu_{10}$ . This approximate correspondence breaks down when  $\epsilon_d$  becomes significant, as  $\epsilon_d$  is set by the detunings  $\delta_0$  and  $\delta_1$ , not  $\Delta\nu_{10}$ . In such scenarios,  $\epsilon_{s,\text{max}}$  can be substantially different for chains with different ion separation but the same  $\Delta\nu_{10}$ .

Figure 11 shows the simulated values of  $\epsilon_d$  and  $\epsilon_r$  over a broad range of  $\delta\omega/2\pi$ , for both even  $N$  and odd  $N$ . We see that  $\epsilon_r$  strongly dominates  $\epsilon_d$  when  $N \lesssim 20$  (for even  $N$ ) and when  $N \lesssim 27$  (for odd  $N$ ), except in the small region near  $\delta\omega \approx 0$  where  $\epsilon_r$  is below the  $10^{-7}$  floor in  $\epsilon_d$ . As a result,  $\Delta\nu_{10}$  determines  $\epsilon_{s,\text{max}}$  for these values of  $N$ . However, for  $N$  greater than these values,  $\delta_1$  becomes small enough that  $\epsilon_d$  makes a significant contribution to  $\epsilon_s$ , and the one-to-one correspondence between  $\Delta\nu_{10}$  and  $\epsilon_{s,\text{max}}$  breaks down. Likewise, the crossover point in  $\delta\omega$  at which  $\epsilon_d = \epsilon_r$  can be estimated from Fig. 11. In general, the crossover point depends on the frequency spacing

between the nearest two modes and on the detuning from the nearest mode.

- 
- [1] B. P. Lanyon, C. Hempel, D. Nigg, M. Müller, R. Gerritsma, F. Zähringer, P. Schindler, J. T. Barreiro, M. Rambach, G. Kirchmair, M. Hennrich, P. Zoller, R. Blatt, and C. F. Roos, Universal digital quantum simulation with trapped ions, *Science* **334**, 57 (2011).
  - [2] P. W. Shor, Scheme for reducing decoherence in quantum computer memory, *Phys. Rev. A* **52**, R2493 (1995).
  - [3] A. Kitaev, Fault-tolerant quantum computation by anyons, *Ann. Phys. (N. Y.)* **303**, 2 (2003).
  - [4] D. Aharonov and M. Ben-Or, Fault-tolerant quantum computation with constant error rate, *SIAM J. Comput.* **38**, 1207 (2008).
  - [5] A. Sørensen and K. Mølmer, Entanglement and quantum computation with ions in thermal motion, *Phys. Rev. A* **62**, 022311 (2000).
  - [6] C. J. Ballance, T. P. Harty, N. M. Linke, M. A. Sepiol, and D. M. Lucas, High-fidelity quantum logic gates using trapped-ion hyperfine qubits, *Phys. Rev. Lett.* **117**, 060504 (2016).

- [7] J. P. Gaebler, T. R. Tan, Y. Lin, Y. Wan, R. Bowler, A. C. Keith, S. Glancy, K. Coakley, E. Knill, D. Leibfried, and D. J. Wineland, High-fidelity universal gate set for  $^9\text{Be}^+$  ion qubits, *Phys. Rev. Lett.* **117**, 060505 (2016).
- [8] C. R. Clark, H. N. Tinkey, B. C. Sawyer, A. M. Meier, K. A. Burkhardt, C. M. Seck, C. M. Shappert, N. D. Guise, C. E. Volin, S. D. Fallek, H. T. Hayden, W. G. Rellergert, and K. R. Brown, High-fidelity Bell-state preparation with  $^{40}\text{Ca}^+$  optical qubits, *Phys. Rev. Lett.* **127**, 130505 (2021).
- [9] L. Egan, D. M. Debroy, C. Noel, A. Risinger, D. Zhu, D. Biswas, M. Newman, M. Li, K. R. Brown, M. Cetina, and C. Monroe, Fault-tolerant control of an error-corrected qubit, *Nature* **598**, 281 (2021).
- [10] D. Kielpinski, C. Monroe, and D. J. Wineland, Architecture for a large-scale ion-trap quantum computer, *Nature* **417**, 709 (2002).
- [11] J. M. Pino, J. M. Dreiling, C. Figgatt, J. P. Gaebler, S. A. Moses, M. S. Allman, C. H. Baldwin, M. Foss-Feig, D. Hayes, K. Mayer, C. Ryan-Anderson, and B. Neyenhuis, Demonstration of the trapped-ion quantum CCD computer architecture, *Nature* **592**, 209 (2021).
- [12] S. A. Moses, C. H. Baldwin, M. S. Allman, R. Ancona, L. Ascarrunz, C. Barnes, J. Bartolotta, B. Bjork, P. Blanchard, M. Bohn, J. G. Bohnet, N. C. Brown, N. Q. Burdick, W. C. Burton, and S. L. Campbell *et al.*, A race-track trapped-ion quantum processor, *Phys. Rev. X* **13**, 041052 (2023).
- [13] B. P. Ruzic, T. A. Barrick, J. D. Hunker, R. J. Law, B. K. McFarland, H. J. McGuinness, L. P. Parazzoli, J. D. Sterk, J. W. Van Der Wall, and D. Stick, Entangling-gate error from coherently displaced motional modes of trapped ions, *Phys. Rev. A* **105**, 052409 (2022).
- [14] J. K. Iverson and J. Preskill, Coherence in logical quantum channels, *New J. Phys.* **22**, 073066 (2020).
- [15] Y. Wang, S. Crain, C. Fang, B. Zhang, S. Huang, Q. Liang, P. H. Leung, K. R. Brown, and J. Kim, High-fidelity two-qubit gates using a microelectromechanical-system-based beam steering system for individual qubit addressing, *Phys. Rev. Lett.* **125**, 150505 (2020).
- [16] S. Debnath, N. M. Linke, C. Figgatt, K. A. Landsman, K. Wright, and C. Monroe, Demonstration of a small programmable quantum computer with atomic qubits, *Nature* **536**, 63 (2016).
- [17] K. Wright, K. M. Beck, S. Debnath, J. M. Amini, Y. Nam, N. Grzesiak, J.-S. Chen, N. C. Plesenti, M. Chmielewski, C. Collins, K. M. Hudek, J. Mizrahi, J. D. Wong-Campos, S. Allen, and J. Apsdorf *et al.*, Benchmarking an 11-qubit quantum computer, *Nat. Commun.* **10**, 5464 (2019).
- [18] S.-L. Zhu, C. Monroe, and L.-M. Duan, Arbitrary-speed quantum gates within large ion crystals through minimum control of laser beams, *Europhys. Lett. (EPL)* **73**, 485 (2006).
- [19] C. F. Roos, Ion trap quantum gates with amplitude-modulated laser beams, *New J. Phys.* **10**, 013002 (2008).
- [20] J. Benhelm, G. Kirchmair, C. F. Roos, and R. Blatt, Towards fault-tolerant quantum computing with trapped ions, *Nat. Phys.* **4**, 463 (2008).
- [21] T. Choi, S. Debnath, T. A. Manning, C. Figgatt, Z.-X. Gong, L.-M. Duan, and C. Monroe, Optimal quantum control of multimode couplings between trapped ion qubits for scalable entanglement, *Phys. Rev. Lett.* **112**, 190502 (2014).
- [22] H. N. Tinkey, C. R. Clark, B. C. Sawyer, and K. R. Brown, Transport-enabled entangling gate for trapped ions, *Phys. Rev. Lett.* **128**, 050502 (2022).
- [23] D. Leibfried, E. Knill, C. Ospelkaus, and D. J. Wineland, Transport quantum logic gates for trapped ions, *Phys. Rev. A* **76**, 032324 (2007).
- [24] P. H. Leung, K. A. Landsman, C. Figgatt, N. M. Linke, C. Monroe, and K. R. Brown, Robust 2-qubit gates in a linear ion crystal using a frequency-modulated driving force, *Phys. Rev. Lett.* **120**, 020501 (2018).
- [25] V. M. Schäfer, C. J. Ballance, K. Thirumalai, L. J. Stephenson, T. G. Ballance, A. M. Steane, and D. M. Lucas, Fast quantum logic gates with trapped-ion qubits, *Nature* **555**, 75 (2018).
- [26] P. H. Leung and K. R. Brown, Entangling an arbitrary pair of qubits in a long ion crystal, *Phys. Rev. A* **98**, 032318 (2018).
- [27] K. A. Landsman, Y. Wu, P. H. Leung, D. Zhu, N. M. Linke, K. R. Brown, L. Duan, and C. Monroe, Two-qubit entangling gates within arbitrarily long chains of trapped ions, *Phys. Rev. A* **100**, 022332 (2019).
- [28] R. Blümel, N. Grzesiak, N. Plesenti, K. Wright, and Y. Nam, Power-optimal, stabilized entangling gate between trapped-ion qubits, *npj Quantum Inf.* **7**, 147 (2021).
- [29] M. Kang, Y. Wang, C. Fang, B. Zhang, O. Khosravani, J. Kim, and K. R. Brown, Designing filter functions of frequency-modulated pulses for high-fidelity two-qubit gates in ion chains, *Phys. Rev. Appl.* **19**, 014014 (2023).
- [30] T. J. Green and M. J. Biercuk, Phase-modulated decoupling and error suppression in qubit-oscillator systems, *Phys. Rev. Lett.* **114**, 120502 (2015).
- [31] Y. Lu, S. Zhang, K. Zhang, W. Chen, Y. Shen, J. Zhang, J.-N. Zhang, and K. Kim, Global entangling gates on arbitrary ion qubits, *Nature* **572**, 363 (2019).
- [32] A. R. Milne, C. L. Edmunds, C. Hempel, F. Roy, S. Mavadia, and M. J. Biercuk, Phase-modulated entangling gates robust to static and time-varying errors, *Phys. Rev. Appl.* **13**, 024022 (2020).
- [33] Y. Shapira, R. Shaniv, T. Manovitz, N. Akerman, and R. Ozeri, Robust entanglement gates for trapped-ion qubits, *Phys. Rev. Lett.* **121**, 180502 (2018).
- [34] Y. Shapira, R. Shaniv, T. Manovitz, N. Akerman, L. Peleg, L. Gazit, R. Ozeri, and A. Stern, Theory of robust multi-qubit nonadiabatic gates for trapped ions, *Phys. Rev. A* **101**, 032330 (2020).
- [35] M. Kang, Q. Liang, B. Zhang, S. Huang, Y. Wang, C. Fang, J. Kim, and K. R. Brown, Batch optimization of frequency-modulated pulses for robust two-qubit gates in ion chains, *Phys. Rev. Appl.* **16**, 024039 (2021).
- [36] Z. Jia, S. Huang, M. Kang, K. Sun, R. F. Spivey, J. Kim, and K. R. Brown, Angle-robust two-qubit gates in a linear ion crystal, *Phys. Rev. A* **107**, 032617 (2023).
- [37] S. M. Clark, D. Lobser, M. C. Revelle, C. G. Yale, D. Bossert, A. D. Burch, M. N. Chow, C. W. Hogle, M. Ivory, J. Pehr, B. Salzbrenner, D. Stick, W. Sweatt, J. M. Wilson, E. Winrow, and P. Maunz, Engineering the quantum scientific computing open user testbed, *IEEE Trans. Quantum Eng.* **2**, 1 (2021).
- [38] C. D. Bruzewicz, J. M. Sage, and J. Chiaverini, Measurement of ion motional heating rates over a range

- of trap frequencies and temperatures, *Phys. Rev. A* **91**, 041402(R) (2015).
- [39] I. A. Boldin, A. Kraft, and C. Wunderlich, Measuring anomalous heating in a planar ion trap with variable ion-surface separation, *Phys. Rev. Lett.* **120**, 023201 (2018).
- [40] M. A. Nielsen, A simple formula for the average gate fidelity of a quantum dynamical operation, *Phys. Lett. A* **303**, 249 (2002).
- [41] K. Kim, M.-S. Chang, R. Islam, S. Korenblit, L.-M. Duan, and C. Monroe, Entanglement and tunable spin-spin couplings between trapped ions using multiple transverse modes, *Phys. Rev. Lett.* **103**, 120502 (2009).
- [42] C. A. Sackett, D. Kielpinski, B. E. King, C. Langer, V. Meyer, C. J. Myatt, M. Rowe, Q. A. Turchette, W. M. Itano, D. J. Wineland, and C. Monroe, Experimental entanglement of four particles, *Nature* **404**, 256 (2000).
- [43] T. A. Manning, *Quantum Information Processing with Trapped Ion Chains*, Ph.D. thesis, University of Maryland, College Park, 2014.
- [44] C. Figgatt, A. Ostrander, N. M. Linke, K. A. Landsman, D. Zhu, D. Maslov, and C. Monroe, Parallel entangling operations on a universal ion-trap quantum computer, *Nature* **572**, 368 (2019).
- [45] G.-D. Lin, S.-L. Zhu, R. Islam, K. Kim, M.-S. Chang, S. Korenblit, C. Monroe, and L.-M. Duan, Large-scale quantum computation in an anharmonic linear ion trap, *EPL (Europhys. Lett.)* **86**, 60004 (2009).
- [46] M. Johanning, Isospaced linear ion strings, *Appl. Phys. B* **122**, 71 (2016).
- [47] Y. Xie, X. Zhang, B. Ou, T. Chen, J. Zhang, C. Wu, W. Wu, and P. Chen, Creating equally spaced linear ion string in a surface-electrode trap by feedback control, *Phys. Rev. A* **95**, 032341 (2017).
- [48] S. Crain, E. Mount, S. Baek, and J. Kim, Individual addressing of trapped  $^{171}\text{Yb}^+$  ion qubits using a microelectromechanical systems-based beam steering system, *Appl. Phys. Lett.* **105**, 181115 (2014).
- [49] C. Fang, Y. Wang, S. Huang, K. R. Brown, and J. Kim, Crosstalk suppression in individually addressed two-qubit gates in a trapped-ion quantum computer, *Phys. Rev. Lett.* **129**, 240504 (2022).